

**COUPLING OF SOLID-STATE AND ELECTROMAGNETIC
EQUATIONS FOR THE COMPUTATIONALLY EFFICIENT TIME-
DOMAIN MODELING AND DESIGN OF WIRELESS PACKAGED
GEOMETRIES WITH NONLINEAR\ACTIVE DEVICES**

A Thesis
Presented to
The Academic Faculty

by

Brian S. McGarvey

In Partial Fulfillment
of the Requirements for the Degree
Master of Science in the
School of Electrical and Computer Engineering

Georgia Institute of Technology
May 2007

**COUPLING OF SOLID-STATE AND ELECTROMAGNETIC
EQUATIONS FOR THE COMPUTATIONALLY EFFICIENT TIME-
DOMAIN MODELING AND DESIGN OF WIRELESS PACKAGED
GEOMETRIES WITH NONLINEAR\ACTIVE DEVICES**

Approved by:

Dr. Manos Tentzeris, Advisor
School of Electrical and Computer Engineering
Georgia Institute of Technology

Dr. Joy Laskar
School of Electrical and Computer Engineering
Georgia Institute of Technology

Dr. John Papapolymerou
School of Electrical and Computer Engineering
Georgia Institute of Technology

Date Approved: Apr 8, 2007

*For my parents
My journey has been long, and I have enjoyed the trip.*

*For my beautiful wife and wonderful children
I love you!*

ACKNOWLEDGEMENTS

Special Thanks to Dr. Manos Tentzeris for being an extremely patient advisor allowing me enough latitude to both explore this material and time to complete the study.

My wife, daughter, and unborn child for their special understanding of the time required to complete this very long project.

Russ Gartman for his patience during the many hours discussion regarding hydrodynamics to reach some of the conclusions contained within this thesis.

TABLE OF CONTENTS

ACKNOWLEDGEMENTS.....	iv
LIST OF FIGURES	viii
LIST OF TABLES	x
LIST OF SYMBOLS.....	xi
SUMMARY	xii
INTRODUCTION	1
CHAPTER 2: HISTORY	3
2.1 Historic Timeline.....	5
CHAPTER 3: LITERATURE REVIEW.....	7
3.1 Balance Equation Model – Hydrodynamic Model	7
3.2 Blotekjaer’s Model.....	10
3.3 Tomizawa’s Model.....	12
3.3.1 Explicit Discretization	13
3.4 El-Ghazaly’s Model	14
3.4.1 El-Ghazaly’s Explicit Discretization Method	16
3.5 Aste and Vahldieck Model.....	17
3.5.1 Aste & Vahldieck Explicit Discretization Method	18
CHAPTER 4: ANALYSIS OF REVIEWED MODELS	20
4.1.1 Speed of Sound	20
4.1.2 Poisson Equation	22
4.1.3 Concentration Gradient Effects	22

4.1.4	Notes Regarding Equations for Model Development	25
4.1.5	Collision Terms $\left(\frac{\partial n}{\partial t}\right)_c, \left(\frac{\partial(n\vec{p})}{\partial t}\right)_c, \left(\frac{\partial(nw)}{\partial t}\right)_c$	26
4.1.6	Relaxation Rates specific to Semiconductor Modeling.....	27
4.2	Electromagnetic Force Equations	28
4.3	Plasma Parameters.....	29
4.3.1	Debye Length- λ_D	30
4.3.2	Plasma Frequency	33
4.3.3	Plasma Parameters Interpretation for Semiconductors.....	34
CHAPTER 5: MODEL COUPLING METHODOLOGY		38
5.1	Physical System Coupling Method.....	39
5.1.1	Picket-May Model Coupling (FDTD-EM & SPICE).....	39
5.1.2	Thevenin Equivalent Model.....	39
5.1.3	Thevenin Equivalent circuit “Looking into” the FDTD lattice.....	40
5.1.4	Lattice Impedance.....	43
5.1.5	Coupling the Models in Time.....	45
5.1.6	Coupling the models in the FDTD-EM grid.....	46
5.1.7	Voltage Excitation Method	47
5.1.8	Current Response	48
CHAPTER 6: HDM MODEL		50
6.1.1	Model Development and Simplification	51
6.2	Discretization.....	54
6.2.1	Gridding Methodology	54
6.2.2	Discretization.....	55

6.2.3	Space and Time Step Disparity.....	57
6.2.4	Excitation Methodology.....	57
CHAPTER 7: RESULTS		60
7.1	Benchmark Diode.....	61
7.2	Initial Conditions.....	62
7.3	Model Stability.....	65
7.4	AC results.....	73
7.4.1	AC excitation method.....	74
7.4.2	Leapfrog Results.....	76
7.4.3	Aste & Vahldieck Upwind Method Results.....	79
7.4.4	Comparison of HDM Discretization Methods.....	82
CONCLUSION.....		86
REFERENCES.....		87

LIST OF FIGURES

Figure 1: Illustration of Gradient Widths	24
Figure 2: Diffusion Current Density Generated by Concentration Gradient	24
Figure 3: Debye Length and Debye Voltage vs. Carrier Concentration	32
Figure 4: Relationship between Debye Length and Potential	33
Figure 5: Plasma Frequency vs. Doping Concentration	34
Figure 6: Plasma Frequency Ballistic Diode vs. Doping Profile	36
Figure 7: Thevenin Equivalent circuit for FDTD-EMS, DS coupling.....	41
Figure 8: Thevenin Equivalent Voltage Loops	42
Figure 9: V-Thevenin Smoothing	44
Figure 10: V-Thevenin Response for $\Delta x_{EMS} / 10$	45
Figure 11: Gridding Method	55
Figure 12: Excitation Methodology	59
Figure 13: Doping Profile	62
Figure 14: Initial Condition for Lax-Wendroff and Leapfrog	64
Figure 15: Initial Carrier distribution for Lax-Wendroff and Leapfrog	64
Figure 16: Initial Carrier Velocity Distribution.....	65
Figure 17: DC bias: Ramp Excitation.....	66
Figure 18: DC bias: Upwind Method Stable but non-convergent.....	67
Figure 19: DC bias: Average Carrier Velocity	68

Figure 20: DC Bias: Carrier Concentration Distribution	69
Figure 21: DC bias: Average Energy	70
Figure 22: DC bias: Total Energy ($n \cdot w$)	70
Figure 23: DC bias: Internal Electric Field	71
Figure 24: DC bias: Internal Voltage.....	71
Figure 25: Current Density Response Lax-Wendroff.....	72
Figure 26: Carrier Concentration Response Lax-Wendroff.....	72
Figure 27: Excitation Methodology	75
Figure 28: 500GHz Excitation Leapfrog Method.....	76
Figure 29: 500GHz Excitation Leapfrog Method.....	77
Figure 30: 100GHz Excitation Leapfrog Method.....	77
Figure 31: 100GHz Response Leapfrog Method	78
Figure 32: 20GHz Excitation Leapfrog Method.....	78
Figure 33: 20GHz Response Leapfrog Method	79
Figure 34: 500GHz Excitation A&V Upwind Method.....	80
Figure 35: 500GHz Excitation A&V Upwind Method.....	80
Figure 36: 100GHz Excitation A&V Upwind Method.....	81
Figure 37: 100GHz Excitation A&V Upwind Method.....	81
Figure 38: 100GHz Response Leapfrog and Upwind Methods	83
Figure 39: Zoomed from previous image.....	84

LIST OF TABLES

Table 1: HDM Gridding.....	84
Table 2: HDM Time steps for RF Excite Tests.....	85
Table 3: Compare HDM and EMS.....	85

LIST OF SYMBOLS

Symbol	Meaning	
n	Average carrier concentration	
\bar{v}_d	Average carrier velocity	
w	Average carrier energy	
m^*	Average carrier effective mass	
\bar{p}_d	Average carrier momentum	
T_e	Average electron gas temperature	
$T_{Lattice}$	Semiconductor lattice temperature	
\bar{q}	Electron gas heat flux	
\vec{F}	Lorentz force acting on plasma	
Φ	Quasi-static voltage potential	
κ	Thermal conductivity of electron gas	
$\nu_p(w)$	Momentum relaxation rate	
$\nu_w(w)$	Energy relaxation rate	
N_D	Density of donors	
N_A	Density of acceptors	
λ_d	Debye Length	
\vec{E}	Electric Field	
\vec{H}	Magnetic Field	
ϵ_r	Effective permittivity	
μ_r	Effective permeability	
Constants		
k_B	Boltzmann's Constant	1.38066e-23 J-s
q, e	Magnitude of electronic charge	1.60219e-19 C
h	Plank's constant	6.62618e-34 J/K
m_o	Rest mass of an electron	9.10953e-31 kg
ϵ_0	Permittivity of free space	8.85419e-12 F/m
μ_0	Permeability of free space	$4\pi \times 10^{-7}$ N·A ⁻²
c	Speed of light in vacuum	2.99792e8 m/s

SUMMARY

This document contains a proposal for the creation of a simulator that can accurately model the interaction of electromagnetic (EM) and semiconductor effects for modern wireless devices including nonlinear and/or active devices.

The proposed simulator couples the balanced semiconductor equations (charge, momentum, kinetic energy) with a FDTD full-wave Yee-based electromagnetic (EM) simulator. The resultant CAD tool is able to model the response of one semiconductor device to both small signal and DC bias based on the process parameters (material, charge distribution and doping) without any *a-priori* knowledge of the device performance characteristics, thus making it extremely useful in modeling and integrating novel devices in RF and Wireless topologies. As a proof of concept an $n^+i^-n^+$ diode will be simulated. In the future, more complicated structures, such as MODFETs, will be modeled as well.

INTRODUCTION

The balanced equation model has been used successfully by several other authors for the simulation of semiconductor devices [1,2,3]. The purpose of this proposal is to increase the breadth of the solution domain and the modeling accuracy using this technique. Tomizawa shows in his book [1] the derivation of the balanced equation model from the Boltzmann's Transport Equation, and the means to calculate the relaxation rates for Silicon and Gallium Arsenide, but his work mainly focused on Monte-Carlo methods of simulation to obtain semiconductor parameterization curves. El-Ghazaly's work shows the co-simulation of a balanced equation model and an FDTD EM model in the same numerical grid, but is severely limited by its excessive computational requirements [2]. McGarvey and Tentzeris demonstrated one method to embed the highly dense grid required for the device simulator into a traditional discretized FDTD-EM simulator and derived an expression for the numerical stability of the co-simulation. This proposal seeks to continue this effort [4].

In detail, this proposal aims to demonstrate and further enhance the capabilities of the numerical techniques described in [1, 2, 4, 5], for a more generic set of devices. To benchmark this novel approach that couples the solid-state and Maxwell equations, a 1-D $n^+ - i - n^+$ Silicon ballistic diode will be tested with a 3D FDTD-EM simulator. This 1D solid-state geometry reduces the multi-dimensional complexity of the device simulator, while maintaining a complete set of boundary conditions and variables that are required to couple the two systems. The developed simulator can be used to incorporate

commonly used feeding and biasing structures, such as Coplanar Waveguides and microstrip lines.

CHAPTER 2: HISTORY

An introduction to the choices made for the simulator integration is necessary to understand the scope of the work proposed here. The stated purpose is to integrate a solid state simulator with an electromagnetic simulator for packaged wireless non-linear devices. This involves choosing an electromagnetic model and a solid state model. The choice for the electromagnetic simulator has been previously made and is the Yee derived Finite Difference Time Domain (FDTD) model [6]. The benefits of FDTD method are well known and understood, and beyond the scope of this proposal. The chosen solid state model is the hydrodynamic model also known as the balanced equation model [1,2,4,5].

Choosing a solid state simulator requires the understanding of device size, and frequency band of interest. The device size depends on the utilized semiconductor fabrication techniques (2004/5: 220nm to 90nm gate lengths). The frequencies of interest in this thesis are within the 1-100GHz range. Models available in literature for device simulations vary from Statistical Quantum Mechanical models [7] to tested device response curves imported from SPICE models [8]. A brief summary describing the most commonly used models is presented below from most to least detailed approximations.

- Single particle quantum mechanical models exist [7,9], but the application of their solutions is not relevant to wireless applications and sizes of interest.
- N-body [10] models, that can fully describe the interactions of the semiconductor lattice, individual charge carriers, and external forces, but fail to adequately describe observed quantum mechanical and thermodynamic effects, such as thermal diffusion.
- Monte-Carlo simulations are often considered the best method for characterizing a device. The method is typically used to obtain very good device response

curves. The computational requirements make it impractical to use in a time domain device simulator. [11,12,13]

- Hydrodynamic models [1,2,4,5], that adequately approximate the individual particle motion of the carriers and lattice and the collective response. This approach allows the device to be co-simulated in an EM simulator without *a priori* knowledge of the device response. It also includes nano-device effects of interest for high frequency devices, such as tunneling and velocity overshoot.
- Drift-Diffusion model [14]; this model is well understood, but limited in usefulness as the model breaks down if device length are small and/or the frequency of interest is high.
- SPICE models; this approach has already been implemented [8] and is useful when the response characteristics of the device is already known for the frequency band of interest.

The selection of the hydrodynamic model provides the means to integrate complex observed solid-state behavior into the predictions for submicron or nano-scale devices. This solid-state model is quite complicated and proper implementation requires a broad understanding of multi-discipline physical effects, but is an extremely comprehensive model for simulating nano-devices. Below is a list of features that the hydrodynamic model includes.

- Statistical and Quantum Mechanical effects: Energy Bands, Change in carrier mass, photon emission, etc
- Single or Dual carrier types (electron, holes)
- Velocity overshoot
- Electron Tunneling
- Internal and External force effects (charged particles, EM fields, gas effects)

Fully realizing all the complexities involved with the hydrodynamic model would require exculpation of a diverse set of topics that is beyond the scope of this work. A partial list and reference materials are supplied for the reader. Following is a partial list of interactions that would need to be considered to determine the limits of a chosen semiconductor simulator: charged particle physics, Electromagnetics, Thermodynamics, Plasma Physics, Quantum mechanics, Statistical mechanics, Astrophysics, and semiconductor physics [15,16,7,17,18,19,20,14, 21].

2.1 Historic Timeline

To firmly establish the validity of the chosen model, a historic timeline showing the development of the balanced equation model as it applies to semiconductors is presented. The basic assumption is that the electron and holes behave consistently with both particle and collective gas effects, as described by Boltzmann and Maxwell [22, 23]. This dual behavior is generally described with the Kinetic Theory of Gases, and the origin for science of statistical mechanics.

- Bernoulli (1738)
 - Billiard Ball model (Basis for Kinetic Theory of Gases)
 - Heat is nothing more than atomic motion – Later this was determined to be an unacceptable assumption
- John Herapath (1820, 1821)
 - Formal introduction to Kinetic Theory of Gasses
 - Rejected by Humphry Dutz of Royal Society – Too speculative
- Joule, Maxwell, Laplace, Poisson, Carnot, Clapeyron (1840-1855)
 - Develop formalized Caloric Theory
- Maxwell (1858)
 - Develops Mean Free Path theory, builds on Herapath's work
 - Describes Theory of diffusion, viscosity, and Heat Conduction, but failed to predict thermal diffusion
- Maxwell (1859)
 - Hypothesizes that gas viscosity independent of Density, and increases with temperature
- Maxwell (1866)
 - Develops Generalized form for Transport Equation
 - Describes the time it takes for a system to return to equilibrium as "relaxation time"
 - Derives Maxwell Distribution – Probability curve
- Boltzmann (1872)
 - Derives Boltzmann Transport Equation, introduces external forces into Maxwell's Generalized Form
 - Shows that Maxwellian distribution is the only one possible for equilibrium
 - Mathematically proves that H (negative of Entropy) must always decrease or remain constant (equilibrium)
- J D van der Waals (1873)
 - Equations of State, theory concerning continuity of the liquid and gaseous states
- J. Willard Gibbs (1839-1903)
 - Developed Additional Statistical Mechanics from Boltzmann's work – ensemble effects

- Quantum Mechanics (1890+)
 - Plank, Einstein, Bose, Fermi, Dirac, Schrödinger greatly influence Quantum and Statistical mechanics
- Chapman, Enskog (1916, 1917)
 - Shows that thermal diffusion not predicted by Maxwell's general transport equation
 - Showed that Maxwell and Boltzmann approaches were equivalent
 - Introduction of Modern Transport Theory
- Vlasov, (1950)
 - Introduces Plasma Physics
 - Balance Equation Model Derived from Boltzmann's Transport Equation
 - Plasma Physics Enters the scene
- Many (1950-1960)
 - Plasma Physics declassified as cold war cools
- Blotekjaer (1970)
 - Shows derivation for two valley semiconductors and derives relaxation time methods that are still in use currently. Describes phenomenological effects described by equations
- Jacoboni (1977)
 - Reviews charge carrier methods
- Brunetti, Jacoboni Reggiani (1981)
 - Compares Experimental and theoretical measurements with Monte-Carlo simulation for Silicon
- Tomizawa (1982)
 - Monte Carlo Simulation of GaAs Diode (n-i-n) 1982
- Y. Lu & El-Ghazaly (1989)
 - Time Domain Finite Difference Study of Hot carrier Transport in GaAs on sub-picosecond scale.
- Stewart, Ye, Churchill (1988)
 - Improve relaxation rate approximations
- Stewart (1989)
 - Improved Relaxation time formulation of collision terms for 2 band hydrodynamic models
- Tomizawa (1993)
 - Shows derivation related to Balance Equation Model (Book)
- M. A. Alsunaidi , El-Ghazaly (1994)
 - Introduces a coupled FDTD & DS system (FET), EM & device simulator require unified grid
- McGarvey, Tentzeris (2001)
 - Show CFL condition
 - Hypothesizes split grid between the system, and Leapfrog gridding
 - Hypothesizes multi-resolution technique
- Aste, Vahldieck (2004)
 - Present Semi-implicit Upwind scheme for GaAs ballistic diode
 - Present single gas model for GaAs ballistic diode
- McGarvey, Tentzeris (2006) MWCL Submission
 - Present results for Leapfrog method for Ballistic diode
 - Present results for decoupled grids between EM tool and device simulator

CHAPTER 3: LITERATURE REVIEW

The balanced equation model is also known as a “hydrodynamic model” in the published literature. By selecting the hydrodynamic model (HDM) a wider set of sub-micron or nano-scale effects can be included in the simulation gaining a more accurate picture of device characteristics *in-situ*. The HDM is derived from the Boltzmann Transport Equation (BTE) by taking the first three moments in velocity or momentum space. Full derivations can be found in several textbooks [1, 16]. Tomizawa’s derivation is specifically targeted for semiconductors. The HDM model is used to simulate diverse topics such as groundwater flow, space plasma flow, and plasma flow for fusion reactions. Its applicability to solid-state devices is based upon well accepted previous work by Tomizawa, El-Ghazaly, and Aste & Vahldieck [1, 2, 24]. The next section shows the basic model as derived for semiconductor flow.

3.1 Balance Equation Model – Hydrodynamic Model

As the underlying theory behind the plasma and semiconductor models, an introduction to the equation is appropriate. BTE was originally developed in the 1800’s to describe specific observed effects in dilute gasses and to expand the Kinetic Theory of Gasses. The model has found wide use in physical models that describe the physical effects in systems that contain gradients and motion. Specifically, the Boltzmann Transport Equation describes a density distribution function f , such that $f(\vec{r}, \vec{v}, t) d\vec{r} d\vec{v}$ denotes the number of particles at time t situated at \vec{r} and have velocity \vec{v} ; the six-dimensional space that describes $\{\vec{r}, \vec{v}\}$ is referred to as

“ μ space”, by Boltzmann. The equation relates the rate of change of the density distribution function to the drift (D) and collision (C) rates, as determined by the system.

Boltzmann’s Transport Equation

$$\frac{\partial f}{\partial t} = -\left(\frac{\partial f}{\partial t}\right)_D + \left(\frac{\partial f}{\partial t}\right)_C \quad (1)$$

f : Velocity density distribution function

t : Time variable

D: drift term

C: collision term

Conservation of Mass, 0th moment

$$\frac{\partial n}{\partial t} = -\nabla \cdot (\vec{v}_d n) + \left(\frac{\partial n}{\partial t}\right)_C \quad (2)$$

Expanding the second gradient term leads to

$$\frac{\partial n}{\partial t} = -((n\nabla \cdot \vec{v}_d) + (\vec{v}_d \cdot \nabla n)) + \left(\frac{\partial n}{\partial t}\right)_C \quad (3)$$

n : carrier concentration

v_d : average drift velocity

Note: This equation describes a compressible fluid, as expected and is parabolic

Conservation of Momentum, 1st Moment

$$\frac{\partial(n\vec{p})}{\partial t} = -\nabla \cdot (n\vec{v}_d \vec{p}_d) + en\vec{F} - \nabla(nk_B T) + \left(\frac{\partial(n\vec{p})}{\partial t}\right)_C \quad (4)$$

n : carrier concentration
 \vec{v}_d : average carrier drift velocity
 \vec{p}_d : average carrier momentum
 k_B : Boltzmann's Constant
 T : electron gas Temperature (K)
 \vec{F} : Lorentz Force

Conservation of Energy, 2nd Moment

$$\frac{\partial(nw)}{\partial t} = -\nabla \cdot (n\vec{v}_d w + \vec{v}_d n k_B T + n\vec{q}) + e\vec{F} \cdot \vec{v}_d n + \left(\frac{\partial(nw)}{\partial t} \right)_C \quad (5)$$

\vec{q} : Heat flux of the electron gas
 Approximated by Fourier's Law

$$n\vec{q} = -\kappa \nabla T \quad (6)$$

The heat conductivity is approximated by the Franz- Wiedemann Law

$$\kappa = \frac{5k_B n T}{2m^* \nu_p(w)} \quad (7)$$

Conservation of Energy, 2nd Moment equation

$$\frac{\partial(nw)}{\partial t} = -\nabla \cdot (n\vec{v}_d w + \vec{v}_d n k_B T - \kappa \nabla T) + e\vec{F} \cdot \vec{v}_d n + \left(\frac{\partial(nw)}{\partial t} \right)_C \quad (8)$$

n : carrier concentration
 \vec{v}_d : average carrier drift velocity
 \vec{q} : Heat Flux
 k_B : Boltzmann's Constant
 T : electron gas Temperature (K)
 κ : thermal conductivity
 m^* : carrier effective mass
 $\nu_p(w)$: Momentum Relaxation Rate

3.2 Blotekjaer's Model

Blotekjaer's Model, printed in 1972, was the first to derive the conservation equations from the BTE without imposing any assumptions on the distribution function, enabling it to be valid for arbitrary band structures, provided the carrier mass was position independent[5]. This model was presented as a 2-valley simulator for GaAs in 1D. The method was meant for analytical investigation, but has become the foundation for most numerical time-domain techniques. The collision terms were complex and later formed the basis for the Baccarani-Wordemann [25] closed form used in this work. The original formulations can be found in [26]¹.

$$\frac{\partial n_i}{\partial t} + \nabla \cdot (\mathbf{v}_i n_i) = \left(\frac{\partial n_i}{\partial t} \right)_C \quad (9)$$

$$\frac{\partial \vec{p}_i}{\partial t} + \nabla \cdot (\mathbf{v}_i \vec{p}_i) = en_i \vec{E} - \nabla (n_i k_B T_i) + \left(\frac{\partial \vec{p}_i}{\partial t} \right)_C \quad (10)$$

$$\frac{\partial (W_i)}{\partial t} + \nabla \cdot (\mathbf{v}_i W_i) = en_i \mathbf{v}_i \cdot \vec{E} + -\nabla \cdot (\vec{v}_d n k_B T) - \nabla \cdot \vec{q}_i + \left(\frac{\partial W_i}{\partial t} \right)_C \quad (11)$$

Key substitutions

Large Plasma Approximation of the Pressure Tensor

$$\nabla \cdot (\mathbf{v}_i \vec{p}_i) \Rightarrow \mathbf{v}_i \cdot \nabla v_i \quad (12)$$

Fourier's Law for heat flux

$$\vec{q}_i = -\kappa_i \nabla T_i \quad (13)$$

Total Energy relation from Kinetic Theory of Gasses

$$W_i = \frac{3}{2} n_i k_B T_i + \frac{1}{2} m_i v_i^2 \quad (14)$$

¹ Blotekjaer references a paper this author has been unable to obtain:

K. Blotekjaer, "High-frequency conductive, carrier waves, and acoustic amplification in drifted semiconductor plasmas," *Ericsson Technics*, vol. 22, pp 125-183, Oct 1966

Average carrier Energy

$$n_i w_i = W_i \quad (15)$$

$$w_i = \frac{3}{2} k_B T_i + \frac{1}{2} m_i v_i^2 = \frac{W_i}{n_i} \quad (16)$$

Total Momentum

$$m_i n_i v_i = \vec{p} \quad (17)$$

With these substitutions, the final transport equations became

$$\frac{\partial n_i}{\partial t} + v_i \cdot \nabla n_i = -n_i \nabla \cdot v_i + \left(\frac{\partial n_i}{\partial t} \right)_c \quad (18)$$

$$\begin{aligned} \frac{\partial v_i}{\partial t} + v_i \cdot \nabla v_i = \\ \frac{e\vec{E}}{m_i} - \frac{2}{3m_i n_i} \nabla(n_i w_i) + \frac{1}{3n_i} \nabla(n_i v_i^2) + \left(\frac{\partial v_i}{\partial t} \right)_c \end{aligned} \quad (19)$$

$$\begin{aligned} \frac{\partial(w_i)}{\partial t} + v_i \cdot \nabla(w_i) = \\ e v_i \cdot \vec{E} + -\frac{2}{3n_i} \nabla \cdot \left[\left(n_i v_i - \frac{\kappa_i}{k_B} \nabla \right) \left(w_i - \frac{1}{2} m_i v_i^2 \right) \right] + \left(\frac{\partial w_i}{\partial t} \right)_c \end{aligned} \quad (20)$$

The key substitutions and assumptions he made were sufficient and valid for the state of the art in semiconductor fabrication in 1972. He analyzed the pressure tensor and found on the scales he was concerned with the large plasma approximation was valid [16,27].

Large Plasma Approximation of the Pressure Tensor

$$\nabla \cdot (v_i \vec{p}_i) \Rightarrow v_i \cdot \nabla v_i \quad (21)$$

The assumption states the spatial variation of the carrier concentration or concentration gradient in the conservation of velocity equation is small and does not contribute to the solution significantly; additionally the mass is position independent leaving the term as

$\nabla \cdot (v_i \vec{v}_i)$ and finally approximated as: $v_i \cdot \nabla v_i$. The secondary effect of the large plasma approximation is the removal of the pressure tensor as the primary means for rotation to be introduced into the fluid flow. Fluid rotation due to the concentration gradient of flow divergence is an important expected effect. The model was originally developed to study ballistic or “Gunn” diodes, due to the fact that excluding the primary means of inducing fluid rotation would make the results easier to study. Blotekjaer’s model has been used by a wide variety of authors to simulate ballistic diodes and other semiconductor devices, but mostly for steady state solutions. Blotekjaer made no attempt to numerically simulate his model.

3.3 Tomizawa’s Model

Tomizawa used Blotekjaer’s work as the foundation for his models. He also utilized the large plasma approximation and constant mass in the final formulations of his model. Most of his work was performed during the early 1990’s; during this timeframe the large plasma approximation was still valid for production level semiconductors. He developed the first two carrier models based on the HDM (holes and electrons). He discretized the equations on a uniform grid using Forward Time Center Spacing (FTCS) discretization method. To achieve the desired results he used a semi-implicit Crank-Nicolson method to achieve stability in time. He published results for Silicon, GaAs, MOSFETS, and HBT’s in several 1D models. Detailed results for the generally accepted n-i-n benchmark device in Silicon and GaAs models were presented for several methods in one dimension [1]. Tomizawa’s main focus was on Monte Carlo simulations and generating I-V curves for devices. The next section shows excerpts from the text specific to fully-explicit time domain techniques used or evaluated in this work.

3.3.1 Explicit Discretization

Tomizawa spent little time presenting the specifics on the discretization methods used for the explicit methods, as his work leaned more toward semi-implicit or fully implicit methods that are numerically more stable for larger time steps at the expense of computational complexity. The CFL condition limits the time step for fully explicit models with the following relation to maximum average carrier velocity.

$$|v| \frac{\Delta t}{\Delta x} \leq 1 \quad (22)$$

The system is a pure hydrodynamic simulator with all variables lying on the nodal points of the discretization grid using a FTCS method for discretization. The main issue is that the system is only 1st order accurate in time, and is numerically unstable for this fully explicit method. A first attempt to improve the stability was done using an upwind method². The method is numerically stable, but suffers from significant numerical dispersion due to the asymmetric nature of the method. The following equation shows the typical discretization methodology.

$$\vec{v}_i^k L_x^{up}[f_i] = \begin{cases} \vec{v}_i^k \frac{f_i^k - f_{i-1}^k}{\Delta x} & \text{if } v_i \geq 0 \\ \vec{v}_i^k \frac{f_{i+1}^k - f_i^k}{\Delta x} & \text{if } v_i < 0 \end{cases} \quad (23)$$

A more complex method, that is second-order accurate in time and space, is the Lax-Wendroff method. Tomizawa suggest using the Lax-Wendroff method to discretize the conservation of mass and momentum equations because of this 2nd order accuracy in time and space.

² This method was first developed at NASA to deal with shock-waves encountered by super-sonic aircraft.

$$\vec{v}_i^k L_x^{LW} [f_i] = \vec{v}_i^k \frac{f_{i+1}^k - f_{i-1}^k}{\Delta x} - \frac{(\vec{v}_i^k)^2 \Delta t}{2} \frac{f_{i+1}^k - 2f_i^k + f_{i-1}^k}{\Delta x^2} \quad (24)$$

However, none of these suggestions appear to have been implemented as his concentration on the subject tends to be on the Crank-Nicolson method, with a code example being provided for that method.

3.4 El-Ghazaly's Model

El-Ghazaly also continued expanding Blotekjaer's original work. He expanded the solution set by embedding a single band, 2D, GaAs FET into a 3D FDTD-EM tool using a unified grid [2, 28]. El-Ghazaly's model, as presented, in is one of few attempts at coupling a FDTD-EM tool with a hydrodynamic simulator. The basic principles of the method are:

- Apply the DC excitation to the device prior to beginning the AC solution.
- During the DC bias convergence, the Poisson equation is used for HDM
- During the AC portion, Maxwell's Curl Equations are used for the HDM instead of the Poisson equation
- Initial conditions of the device simulator are the steady state solutions for the carrier density, momentum, and energy at each cell
- The EM and device simulator share a unified spatial and temporal gridding
- The cell size for the HDM is typically several orders of magnitude smaller than that of the FDTD-EM simulator
- The response of the device simulator is coupled to the EM tool via the current density at each cell where the FDTD-EM and HDM are co-located
- Only single band solutions are computed, so as the conservation of mass equation includes no collision terms.
- Variable effective mass based on the doping
- On axis pressure tensor terms are included

El-Ghazaly's System of Equations

$$\frac{\partial n}{\partial t} + \nabla(n\vec{v}) = 0 \quad (25)$$

$$\frac{\partial(np_x)}{\partial t} + \nabla(n\vec{v}p_x) = qn[E_x + (\vec{v} \times \vec{B})_x] - \nabla(nkT) - \frac{np_x}{\tau_w} \quad (26)$$

$$\frac{\partial(nw)}{\partial t} + \nabla(n\vec{v}w) = qn\vec{v} \cdot \left(E + (\vec{v} \times \vec{B}) \right) - \nabla \cdot (nkT\vec{v}) - \frac{n(w - w_o)}{\tau_w} \quad (27)$$

Method relating Carrier Flow to Current Density

$$\vec{J}(t) = -qn(t)\vec{v}(t) \quad (28)$$

Poisson Equation – Used only during DC solution

$$\frac{\nabla^2 \phi}{\partial x^2} = \frac{q}{\epsilon_o \epsilon_r} (N_D - n_i) \quad (29)$$

Maxwell's Curl Equations – Used for FDTD-EM (AC solution)

$$\nabla \times \vec{E} = -\mu \frac{\partial \vec{H}}{\partial t} \quad (30)$$

$$\nabla \times \vec{H} = -\epsilon \frac{\partial \vec{E}}{\partial t} + \vec{J} \quad (31)$$

In previous approaches, the magnetic field effects were omitted from the Lorentz forces included in the HDM model. Because El-Ghazaly co-located the HDM and FDTD-EM models in a unified grid, he required a technique to calculate the magnetic field in the semiconductor. The effect of the incident Magnetic field should be small compared to the Electric field; detailed analysis of the magnetic field effects on plasmas can be found in other texts on plasma physics [20,29].

Additionally, most hydrodynamic simulators assume a constant effective mass of the carriers [1, 25,30]. El-Ghazaly introduced some variation of the carrier effective mass by introducing variability in the low-field electron mobility (32). This feeds back into the calculation for the effective mass used in equations (26, 27) and in the relaxation rates.

$$m_{eo} = \frac{8000}{1 + \sqrt{N_d / 1 \times 10^{17}}} \quad (32)$$

A significant limit, in the works published by El-Ghazaly, is the lack of a collision term for the conservation of mass. The lack of a collision term explicitly states that only single valley / band devices are being simulated. Also, generation and recombination sites are summarily excluded (typical of most device simulators). El-Ghazaly's model has been used to simulate GaAs structures (typically 2 valley / band structures); as such, the result's accuracy is questionable.

3.4.1 El-Ghazaly's Explicit Discretization Method

El-Ghazaly states in the published works related to the HDM model, the Debye length is the main criterion that determines the maximum cell size for the unified grid. El-Ghazaly does not explicitly state the time step is determined by the plasma frequency of the semiconductor, but the published works do state the time step is on the order of 10^{-17} s which is consistent with expected values when the plasma frequency is used to determine the time step. The result of this approach is a grid that is unified in both time and space, making it exceedingly fine and limiting its usefulness to device sized structures, as is evident by the published results.

The method used to discretize the system of equations utilizes both a Lax method and an upwind method. The Lax method is used for the conservation of momentum; it has a stencil covering two time and space steps for the velocity gradient terms in the momentum equation. The conservation of mass (continuity) and energy equations are discretized with the upwind scheme for "...best accuracy and stability..." [2]. El-Ghazaly

goes on to state there is no gain in using semi-implicit or fully implicit schemes with the small time step ($\Delta t = 10^{-17} s$).

3.5 Aste and Vahldieck Model

The Aste & Vahldieck model is only concerned with the hydrodynamic portion of the combined model, but represents the generally accepted state-of-the-art model [24, 30]. Their model uses a slightly different notation but is very similar to the Blotekjaer, Tomizawa, and El-Ghazaly model. They do not make the large plasma approximation, but they instead apply the product rule to the didactic multiplication in the concentration and velocity gradient term: the pressure tensor. The equations are presented in (33-40) as published including typographical errors.

$$\frac{\partial n}{\partial t} + \nabla(\vec{j}) = 0 \quad (33)$$

$$\frac{\partial(\vec{j})}{\partial t} + (\nabla\vec{j})\vec{v} + (\vec{j}\nabla)\vec{v} = -\frac{e}{m}n\vec{E} - \frac{e}{m}\nabla\left(\frac{nkT}{e}\right) - \frac{\vec{j}}{\tau_p} \quad (34)$$

$$\frac{\partial w}{\partial t} + \nabla(\vec{v}w) = qn\vec{v}\vec{E} - \nabla(\kappa\nabla T) - \frac{n(w - (3/2)nkT_L)}{\tau_w} \quad (35)$$

$$\nabla(\varepsilon\nabla\Phi) = e(n - N_{Di}) \quad (36)$$

$$\vec{E} = -\nabla\Phi \quad (37)$$

$$\Phi : \text{Quasi - static voltage potential} \quad (38)$$

Particle Density

$$\vec{j} = n\vec{v} \quad (39)$$

Particle Density is related to current density by the relation

$$\vec{J} = -e\vec{j} \quad (40)$$

The notation used by Aste and Vahldieck is non-standard, but close examination reveals that the pressure tensor is included without the large plasma approximation, similar to El-Ghazaly's model. The early model [24] paper only describes a 1D simulation, the later model explicitly calls out the inclusion of the off-axis terms in the pressure tensor [30]. The model used in [24] is considered a good benchmarking case for this thesis. This model agrees well with other models, includes a partially staggered grid, and has well documented results. The Aste & Vahldieck model improves on El-Ghazaly's model by specifically including the off-axis terms in the pressure tensor for 2D. The model accuracy is weakened by the asymmetric upwind discretization method used to improve the numerical stability.

3.5.1 Aste & Vahldieck Explicit Discretization Method

Aste and Vahldieck use an offset grid in space to initially setup the discretization grid. The vectors are placed on the nodal points and the scalars are placed on the $\frac{1}{2}$ nodal points, but at the same time point indicating no leapfrogging in time. The method is second order in space, but only first order in time. The authors cite mention stability issues, and impose the upwind scheme (41-43) on several variables in the model to increase the numerical stability.

$$n_{i+1/2}^t = \left\{ \begin{array}{l} \frac{3}{2} n_i^t - n_{i-1}^t : \vec{j}_{i+1/2}^t > 0 \\ \frac{3}{2} n_{i+1}^t - n_{i+2}^t : \vec{j}_{i+1/2}^t < 0 \end{array} \right\} \quad (41)$$

$$\vec{j}_{i+1/2}^t = \left\{ \begin{array}{l} \frac{3}{2} \vec{j}_{-1/2}^t - \vec{j}_{i-3/2}^t : \vec{j}_{i+1/2}^t > 0 \\ \frac{3}{2} \vec{j}_{i+1/2}^t - \vec{j}_{i+3/2}^t : \vec{j}_{i+1/2}^t < 0 \end{array} \right\} \quad (42)$$

$$w_{i+1/2}^t = \left\{ \begin{array}{l} \frac{3}{2} w_i^t - w_{i-1}^t : \vec{j}_{i+1/2}^t > 0 \\ \frac{3}{2} w_{i+1}^t - w_{i+2}^t : \vec{j}_{i+1/2}^t < 0 \end{array} \right\} \quad (43)$$

Electron Temperature (T) is also defined by an upwind scheme similar to the carrier density and carrier energy methods. The up-wind method is generally used to capture hydrodynamic shockwave effects, but it can also be used to add stability.

CHAPTER 4: ANALYSIS OF REVIEWED MODELS

Several authors have been successful in creating various incarnations of computational BEM / HDM models [1,2,5, 24, 31]. Each model under consideration here has implemented the mass, momentum, and energy conservations with various simplifications and combinations of other effects. Several of the limitations will be corrected in this thesis and the proposed approach will be benchmarked in section with the final simulations. Other more advanced effects such as Lorentz forces, electron trapping, and lattice temperature are omitted from the model under consideration to be studied at a later time.

4.1.1 Speed of Sound

Aste and Vahldieck and other authors have applied the relatively simple upwind scheme to capture the hydrodynamic shock waves in the electron gas. These shock waves are generated locally in the grid as the average electron velocity exceeds the speed of sound internal to the device during the simulation. The speed of sound in the electron in electron gas is typically calculated with (44) for one dimensional approximations or (45) when multi-dimensional approximations are concerned. The 5/3 ratio is the adiabatic constant calculated for the electron gas. More information can be found in textbooks discussing the Kinetic Theory of Gasses [9, 16, 29]

$$c = \sqrt{kT/m} \quad (44)$$

$$c = \sqrt{5kT/3m} \quad (45)$$

Typically, the ratio of the velocity to the average electron speed of sound is referred to as a mach number (46). As the flow approaches the speed of sound bunching of the waves in front of the incident flow or aircraft bunches. Prior to exceeding the speed of sound a Doppler shift occurs, when the speed of sound is exceeded the flow is moving faster than the sound waves can travel and create a shockwave at the leading edge of the flow. The typical example used to illustrate the shockwave is the sonic boom of an aircraft as it passes overhead at Mach 1 or greater. The upwind discretization technique can capture this effect as the derivatives are only defined in the upwind direction no numerical information is transferred to or gained from the downwind direction. The discretization method can give acceptable results for cases where the flow rate is less than the speed of sound, but it suffers from numerical dispersion and other issues shown in the results section.

$$machnumber = \frac{velocity}{speed_of_sound} \quad (46)$$

In semiconductor simulators, the electron flow is expected to exceed the calculated speed of sound from either (44) or (45). This reasoning is cited as the major reason for using methods such as upwind in the discretization of the system. [1,24,30]. A better approach would be to utilize the upwind method only when the flow rate exceeds the speed of sound and a less numerically dispersive method such as leapfrog discretizations in all other areas and times of the simulation. This approach could limit the numerical dispersion typically associated with upwind methods. The interface could be a simple threshold comparison for the calculated speed of sound to the current average carrier velocity (magnitude and direction) for the cell.

4.1.2 Poisson Equation

The Poisson equation is suspected to one of the major sources of instability of the simulated system of solid-state equations. For example, as a voltage is applied to a terminal or port at a particular time step, after the Poisson equation is solved, the entire system “feels” the effects instantaneously. The Poisson equation is an elliptical equation and generally referred to as having an infinite propagation speed as the solution at any time is related to the boundary conditions at the same time [32]. For the simulator discussed here, the actual propagation speed is not quite infinity, as the effects of the newly calculated results are not used until the next time step. This results in a calculable propagation speed of the applied voltage through the device from the device ports (47). As an example the benchmark diode that is presented later has a length of 600nm and a typical HDM time step is 1×10^{-18} seconds resulting in an effective propagation speed of the applied voltage 6×10^{11} m/s throughout the device, which is obviously faster than the speed of light. Current literature on plasma physics strongly advise against using Poisson’s equation to close the hydrodynamic model for just this reason, unless absolutely necessary [16,20,27,29]. Because semiconductors have fixed doping profiles that have significant effects on the characteristics of the devices; the Poisson equation is seen as absolutely necessary.

$$\text{Propagation Speed} = \frac{\text{total device length}}{\Delta t_{HDM}} \quad (47)$$

4.1.3 Concentration Gradient Effects

Figure 1 shows a simplified n-i-n ballistic diode with a source, drain, channel, and the transition regions between them. The change in carrier concentration between the

source and channel or the channel and drain along with the gradient width are the driving factor in determining if the large plasma approximation can be made. Figure 2 is a simplified representation of the diffusive current densities generated across the gradient window shown in Figure 1. For large semiconductor devices, micron length feature sizes, the diffusion generated current densities are small even for large changes in concentration densities as shown in Figure 2. As the feature size of the semiconductor shrinks the gradient widths correspondingly shrink giving rise to significant current densities from the diffusive forces. As the gradient width shrinks, the diffusion-induced current density is directly proportional to the reduction in length (48). In this case, the diffusion force from the concentration gradient can no-longer be omitted as it becomes a significant force in the system. Figure 2 was created with a change in concentration from 1×10^{18} to $2.5 \times 10^{15} \text{ cm}^{-3}$ and for a carrier mobility calculated for a concentration of $1 \times 10^{18} \text{ cm}^{-3}$ with constant carrier mobility for simplicity ($\mu = 272.5 \text{ cm}^2/\text{V}\cdot\text{s}$). The device simulator used an empirical formula for the carrier mobility as opposed to a single value used in the example [2,14,24].

Einstein relation

$$D = \mu_0 \frac{kT}{q} \quad (48)$$

Fick's 1st Law states the flux or the particle-flow rate is proportional to the concentration gradient

Particle Density

$$\vec{j} = -D\nabla n \quad (49)$$

Current Density

$$\vec{J} = q\vec{j} \quad (50)$$

Figure 2 shows that Blotekjaer's simplification was accurate for the time it was introduced; however, for current times with 65-90nm gate lengths possible, the concentration gradient has a significant effect and must be included in the model.

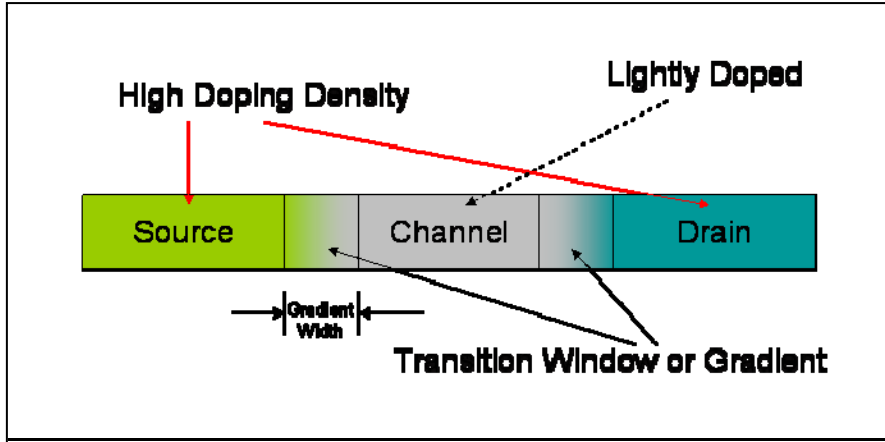


Figure 1: Illustration of Gradient Widths

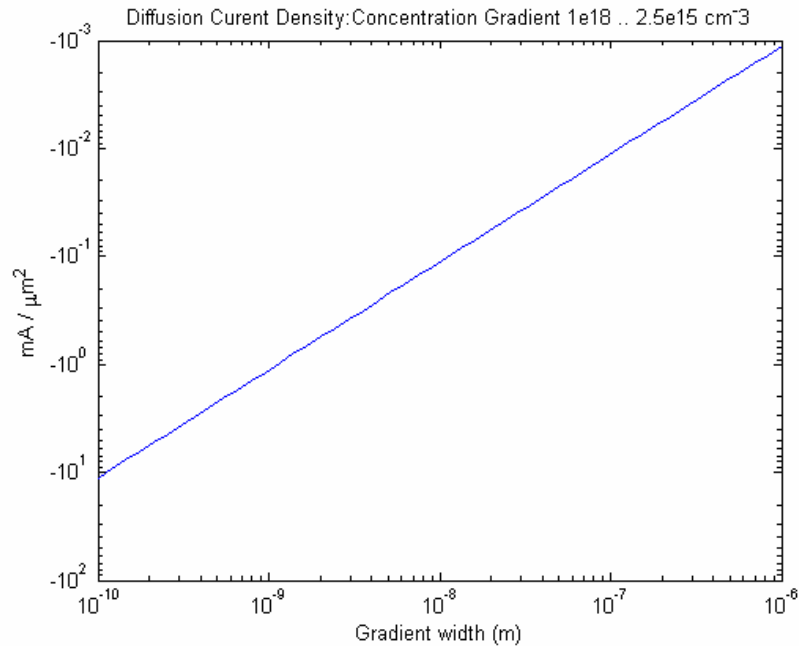


Figure 2: Diffusion Current Density Generated by Concentration Gradient

4.1.4 Notes Regarding Equations for Model Development

The conservation equations presented in (2, 50), (4), and (5) are presented in their most generic forms without any simplification. It has been stated earlier that the hydrodynamic equations are used in a many fields one such example is provided. In aerodynamics the conservation of mass (51) is typically used alone to determine flight or flow characteristics. The governing equation is the Navier-Stokes equation. The Navier-Stokes equation can be derived from the Conservation of Mass equations (51). To derive the Navier-Stokes equation the gas under consideration is considered incompressible. The mathematical representation of this is shown in (52). The resultant equation after (52) is substituted into (51) is the Navier-Stokes equation is produced (53). This small change radically changes the behavior or the system, (53) is incompressible and hyperbolic. Where as, (51) is compressible and parabolic. The hyperbolic equation is more difficult to solve, and has been the source of some confusion in the literature, leading more than one author to address the system as solely hyperbolic causing some concern for the precision of the proposed solutions [1,2, 24].

Conservation of Mass

$$\frac{\partial n}{\partial t} = -((n\nabla \cdot \vec{v}_d) + (\vec{v}_d \cdot \nabla n)) + \left(\frac{\partial n}{\partial t}\right)_c \quad (51)$$

n : carrier concentration

v_d : average drift velocity

Note: This equation describes a compressible fluid, as expected and is parabolic

$$\text{If } \vec{v}_d \cdot \nabla n = 0 \quad (52)$$

The equation (52) describes an incompressible fluid
Also known as the Navier-Stokes Equation which is hyperbolic

$$\frac{\partial n}{\partial t} = -(n\nabla \cdot \vec{v}_d) \quad (53)$$

4.1.5 Collision Terms $\left(\frac{\partial n}{\partial t}\right)_c, \left(\frac{\partial(n\vec{p})}{\partial t}\right)_c, \left(\frac{\partial(nw)}{\partial t}\right)_c$

The final term in each of the derived equations contains a collision term:

$\left(\frac{\partial n}{\partial t}\right)_c, \left(\frac{\partial(n\vec{p})}{\partial t}\right)_c, \left(\frac{\partial(nw)}{\partial t}\right)_c$. Each of these terms describes the losses and gains

associated with collisions for each equation. For example, in the 0th moment, conservation of mass, the collision term describes the loss or gain of mass for the current energy band. This term can relate the transition between energy bands for a carrier, or the source or sink for the boundary conditions, or the recombination and generation of electron-hole pairs within the device for a variety of physical occurrences

[14, 21]. These terms are generally implemented as relaxation rates $1/\tau_n, 1/\tau_p, 1/\tau_w$ [5,

25, 31].

To develop an effective model, the collision terms need to be converted to useable approximations, typically referred to as relaxation rates. Relaxation times, scattering rates, and relaxation rates, all describe the same effect: the means by which particles return to equilibrium after being disturbed. For large plasmas or fluids, the relaxation rates are expressed as viscosity, collision rates, or other terms that relate Newtonian physics terms to the reader. For semiconductors, the relaxation rates are often expressed in terms of semiconductor lattice-particle interaction (phonons), particle to particle scattering, band exchange, or other quantum mechanical effects. The specific methods used to determine these effects are beyond the scope of this paper and as such can be explored in [1, 7, 9, 11]. Several closed form solutions have been presented by [5, 25, 31]. The model presented by Bacarani will be used during this research, as it

is the most widely accepted method. The moment equations have been derived and the relaxation rates have been explained as they generally relate to fluids and plasmas. The paper now shifts in scope from general model development to specific issues concerning its application to semiconductor modeling.

4.1.6 Relaxation Rates specific to Semiconductor Modeling

The relaxation rate, scattering rate, and relaxation time, all relate the same basic physical effects, how collisions change the average density, flow rate, or kinetic energy of the flow. Two basic methods are used to account for this energy loss in the literature. A closed form solution derived from Einstein's relation and the moment expansion or the results of a Monte Carlo simulation. Blotekjaer published the early models and assumptions that were later improved into an approximated closed form solution by Baccaani and Wordemann, who defined relaxation times for silicon with [25].

$$\tau_p = \frac{m}{e} \mu_0 \frac{T_0}{T} \quad (54)$$

$$\tau_w = \frac{m}{e} \mu_0 \frac{T_0}{T} + \frac{3}{2} \frac{k_B}{e v_s^2} \mu_0 \frac{T T_0}{T + T_0} \quad (55)$$

$$\tau_w = \left(\frac{1}{2} + \frac{3 k_B}{2 m_s^2} \frac{T^2}{T + T_0} \right) \tau_p \quad (56)$$

v_s : Saturation velocity at high electric fields

μ_0 : is low field mobility

T : Carrier Temperature

τ_w : Relaxation time for conservation of momentum

τ_p : Relaxation time for conservation of energy

An alternate method, derived from Monte Carlo ensemble particle simulations, may also be used to obtain the relaxation rates of a semiconductor by simulating various DC bias

levels in bulk material and recording the average energy and average velocity of each particle for every time step during the simulation. That information is then tabulated to create an approximation. A lookup table may be used or a closed-form equation approximating the average velocity as a function of energy can be created [1].

The generally accepted practice is to use the Baccarani-Wordemann model derived from Einstein's relation. This method is implemented for all models, simulations, and results presented in this work [1,2,24].

4.2 Electromagnetic Force Equations

Equations (57-59) show the general transport or moment equations. The system still remains under-defined as \vec{F} is an undetermined variable. This force, \vec{F} , describes the Lorentz forces acting on the carriers in the HDM model. This force can be electrostatic, electrodynamic or a combination of the two. Electrostatic effects are coupled into the HDM via Poisson's Equation (60). The electrostatic field is primarily determined by the change in carrier concentration from the original acceptor or donor doping concentration. Electrodynamic effects from Maxwell's curl equations (61-62) are typically ignored in the HDM by omitting them for practical RF devices ($f < 200\text{GHz}$). The fundamental assumption for this simplification is that the excitation is slow in comparison to the response of the device and can be sufficiently coupled via the boundary conditions and the Poisson equation.

There is at least one exception to this generalization. El-Ghazaly presented a coupled FDTD-EM and FDTD-HD model that uses a unified spatial gridding technique. For that

simulator, the DC bias condition is calculated with Poisson's equation for the device initialization, and then Maxwell's curl equations (61) and (62) are used to update the Electric and Magnetic fields inside the device. This and other models will be discussed in the Technical Approach section. Due to the difference in the models, the boundaries of electrostatic and electrodynamic effects of the device simulator have to be explored. As the hydrodynamic model is essentially a plasma approximation, *plasma parameters* are introduced into the discussion. These parameters are typically used to determine the type of plasma and what equations are required to adequately describe the system.

Generalized Transport Equation Set

$$\frac{\partial n}{\partial t} = -((n\nabla \cdot \vec{v}_d) + (\vec{v}_d \cdot \nabla n)) + \left(\frac{\partial n}{\partial t} \right)_c \quad (57)$$

$$\frac{\partial (n\vec{p})}{\partial t} = -\nabla \cdot (n\vec{v}_d \vec{p}_d) + en\vec{F} - \nabla (nk_B T) + \left(\frac{\partial (n\vec{p})}{\partial t} \right)_c \quad (58)$$

$$\frac{\partial (nw)}{\partial t} = -\nabla \cdot (n\vec{v}_d w + \vec{v}_d nk_B T - \kappa \nabla T) + e\vec{F} \cdot \vec{v}_d n + \left(\frac{\partial (nw)}{\partial t} \right)_c \quad (59)$$

Maxwell's Equations

$$\nabla \cdot \vec{E} = \frac{1}{\epsilon_o} \rho_c \quad (60)$$

$$\nabla \times \vec{B} - \frac{1}{c^2} \frac{\partial \vec{E}}{\partial t} = \mu_o \vec{J} \quad (61)$$

$$\nabla \times \vec{E} + \frac{\partial \vec{B}}{\partial t} = 0 \quad (62)$$

$$\nabla \cdot \vec{B} = 0 \quad (63)$$

4.3 Plasma Parameters

The complete set of the four Maxwell's Equations (60-63) describes all possible EM effects for non-dispersive media. However, for typical practical simulations only a subset

of the equations is sufficient for accurate approximations. Common cases of interest include the steady state solution (60) for charge distribution problems. Time varying solutions of electrodynamic problems require only Maxwell's curl equations (61, 62). Both Poisson and Maxwell's curl equation solutions can be used to apply the force to the charged particle or carrier gas of interest in this system, determining if either set or both sets are required to accurately apply the internal/external electromagnetic forces that are acting on the system under investigation. The two governing factors (plasma parameters: the Debye Length and Plasma Frequency) are used in this thesis to determine the correct set of equations to be included in the system. The Debye Length determines if the electrostatic solution is required, (Poisson (60)). The Plasma Frequency along with the maximum frequency of interest in the FDTD-EM model will determine if the electrodynamic effects of the plasma will require the use of Maxwell's curl equations (61, 62) in the simulation. Plasma's are unique in that they can support both longitudinal and transverse electromagnetic waves. The longitudinal waves are typically the electrostatic oscillations; whereas, the transverse waves are traditionally understood as the free-space EM waves propagating through a dispersive media [16,20,27, 37].

4.3.1 Debye Length- λ_D

The Debye length is one of the governing parameters used to justify a particular model's assumptions, and as such requires further explanation.. Many derivations presented often relay little physical understanding [1,14, 20, 33]. The derivation presented below, takes the path from a point charge in a vacuum to a test charge in an ion field, only then showing the relation between the Debye Length and the associated potentials, assisting the reader to gain an intuitive understanding of the Debye length.

Electric Potential due to a point charge in free space [15]

$$V(r) = \frac{1}{4\pi\epsilon_0} \frac{q}{r} \quad (64)$$

$V(r)$ Voltage as a function of radius
 q Electronic Charge
 r Radius
 ϵ_0 Permittivity of free space

Electric Potential due to a point charge in an ionized field [15, 34, 35]

$$V(r) = \frac{Q}{4\pi\epsilon_0 r} e^{-r/\lambda_D} \quad (65)$$

Q Positive Test Charge (+1 * q)
 λ_D Debye Length

Debye Length is defined as [1, 15, 34,35]

$$\lambda_D = \sqrt{\frac{\epsilon_0 kT}{2n_o q^2}} \quad (66)$$

k Boltzmann's Constant
 n_o Carrier Concentration
 T Temperature

Of specific interest to the reader, the field of plasma physics typically uses cgs units, Electrical Engineers typically use MKS, and the semiconductor field uses a combination of cgs and MKS units [36].

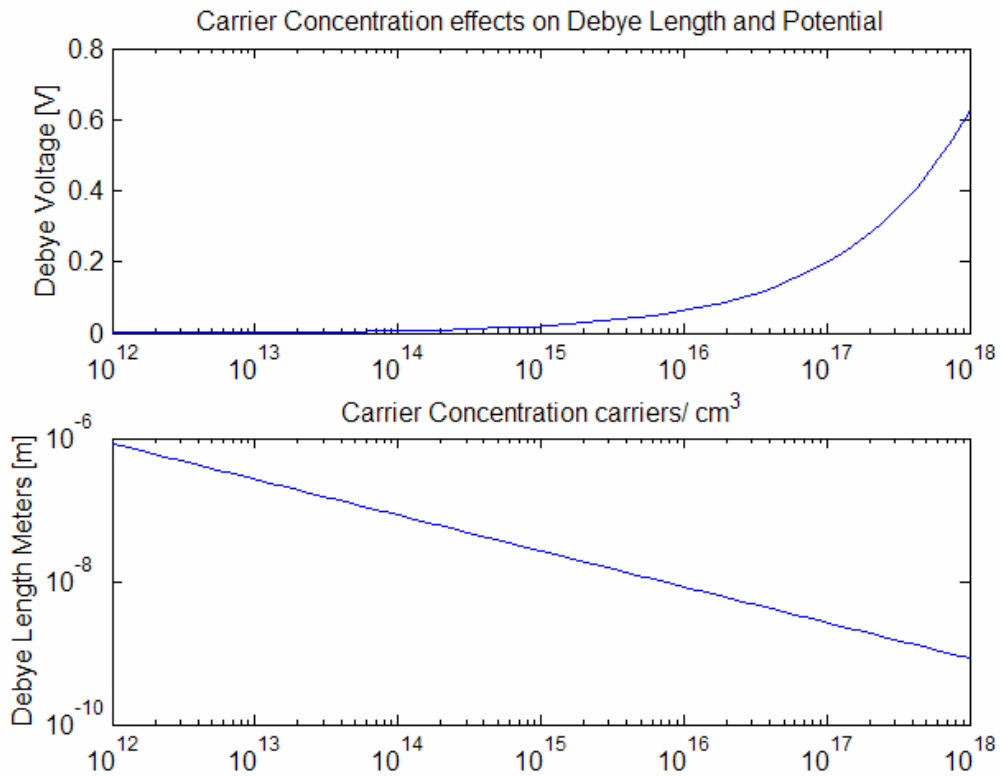


Figure 3: Debye Length and Debye Voltage vs. Carrier Concentration

Figure 3 shows the relationship between the carrier concentration, Debye Voltage and Debye Length, while Figure 4 shows the plot of the Electric Potential due to point charges either in a vacuum or in a charged particle field of a given density. For the particle in vacuum, the potential falls off as expected ($1/r$), but as the charge particle density increases, the voltage falls off dramatically as described by equation (65). The asterisks on the plot show the Debye lengths and the Voltages at which they occur.

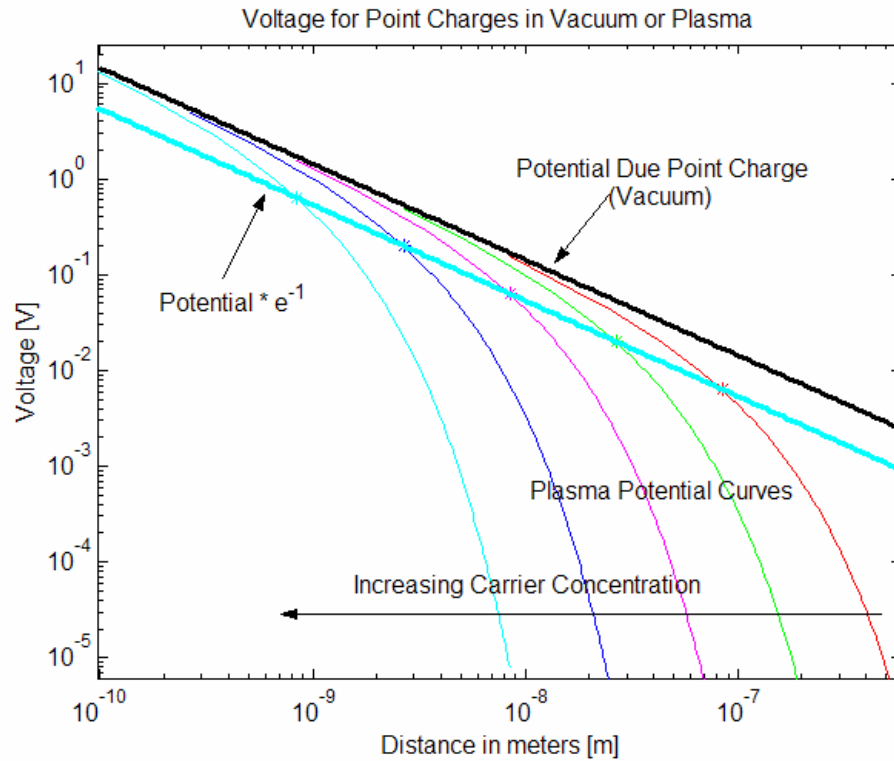


Figure 4: Relationship between Debye Length and Potential

All the Debye Lengths express exactly the distance that the potential has a value equal to e^{-1} , (36.79%, -8.69 dB) of the maximum Voltage of the single test charge. For $3\lambda_D$ the loss is -26.1dB, effectively shielding most local variations in charge densities at high concentrations. The plot visibly shows that as the carrier concentration increases, the Debye Shielding effect rapidly intensifies

4.3.2 Plasma Frequency

The plasma frequency (67) is a commonly used parameter that simply describes a frequency above which plasma can support propagation of a transverse and longitudinal EM wave based mainly on the carrier concentration. Figure 5 shows a plot of the plasma frequency for silicon and GaAs bulk material.

$$2\pi f_p = \omega_p = \sqrt{\frac{e^2 n}{\epsilon_s m^*}} \quad (67)$$

f_p : Plasma Frequency

ω_p : Plasma Frequency

ϵ_s : Dielectric Constant

m^* : Carrier effective mass

n : Carrier Density

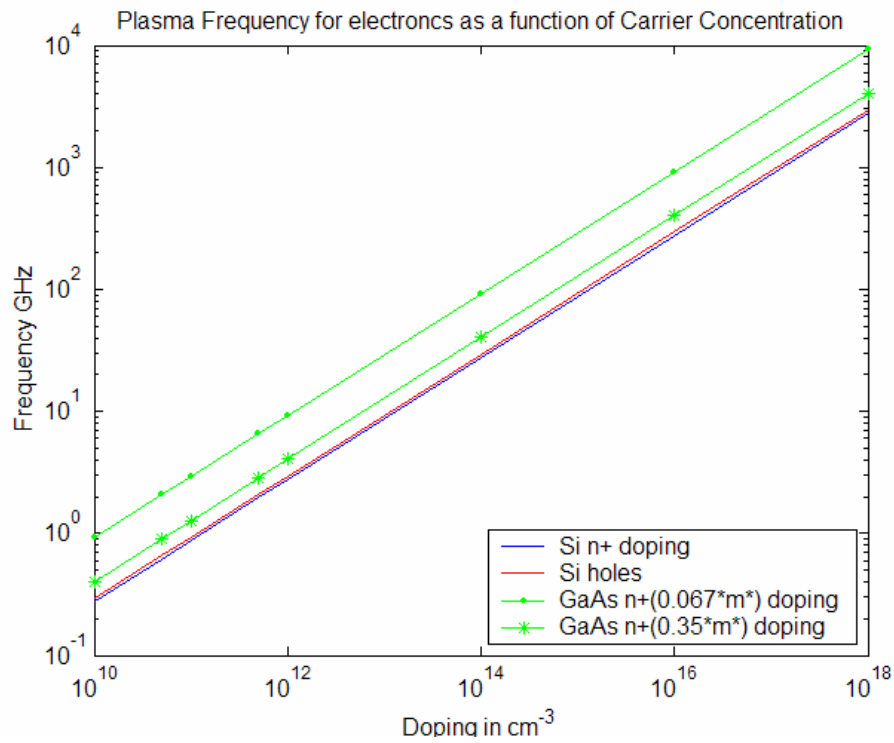


Figure 5: Plasma Frequency vs. Doping Concentration

4.3.3 Plasma Parameters Interpretation for Semiconductors

In astrophysics and nuclear fusion plasma studies, if the length of the plasma under study is sufficiently long, the electrostatic effects can be ignored, else they must be included. The cutoff value for this is usually 3 times the *Debye Length*. Figure 3 shows that for an intrinsic material with a charge density typically 10^{12} cm^{-3} , the Debye Length

is approximately 1micron. But for non-degenerately highly doped material (10^{18} cm^{-3}) the Debye length is on the order of one nanometer. These facts coupled with the known built-in voltages of semiconductors are a very good indication that the electrostatic effects should be included, something that has happened in the presented final model.

The electrodynamic effects on the other side are more difficult to characterize. As a first-order approximation, if the plasma frequency is much larger than the maximum frequency of interest, the FDTD-EM simulator Maxwell's curl equations may be safely ignored. For example, Figure 5 shows that for bulk GaAs and Silicon and frequencies below 10GHz, electrodynamic effects may be omitted with care. The complication comes from the fact that plasmas tend to oscillate at their natural or resonant frequencies, *Plasma Frequency*, when disturbed. EM waves far below the plasma frequency are reflected. EM waves near but below the *Plasma Frequency*, propagate as evanescent waves that quickly die out.

EM waves with a frequency being more than a decade above the plasma frequency propagate through the plasma with little dispersion. However, as stated earlier, plasmas support both longitudinal and transverse electromagnetic waves. The longitudinal waves are typically the electrostatic oscillations; where as, the transverse waves are traditionally understood as EM waves propagating through a dispersive media. This leads to the basic assumption that if the longitudinal waves are to be included, the electrostatic effects must be included as well. Additionally if the incident EM waves are significantly below the plasma frequency of the device, or the transverse waves are not of interest, Maxwell's curl equations can be safely omitted. However, if the transverse waves are of interest, the formulation for Maxwell's curl equations in dispersive media

must be used to capture the plasma effects. Figure 6 shows the minimum plasma frequency to be approximately 1 THz for an example of an *n-i-n* ballistic diode. Since most practical RF devices operate well below that frequency, the curl equations and the dispersive transverse waves can be ignored.

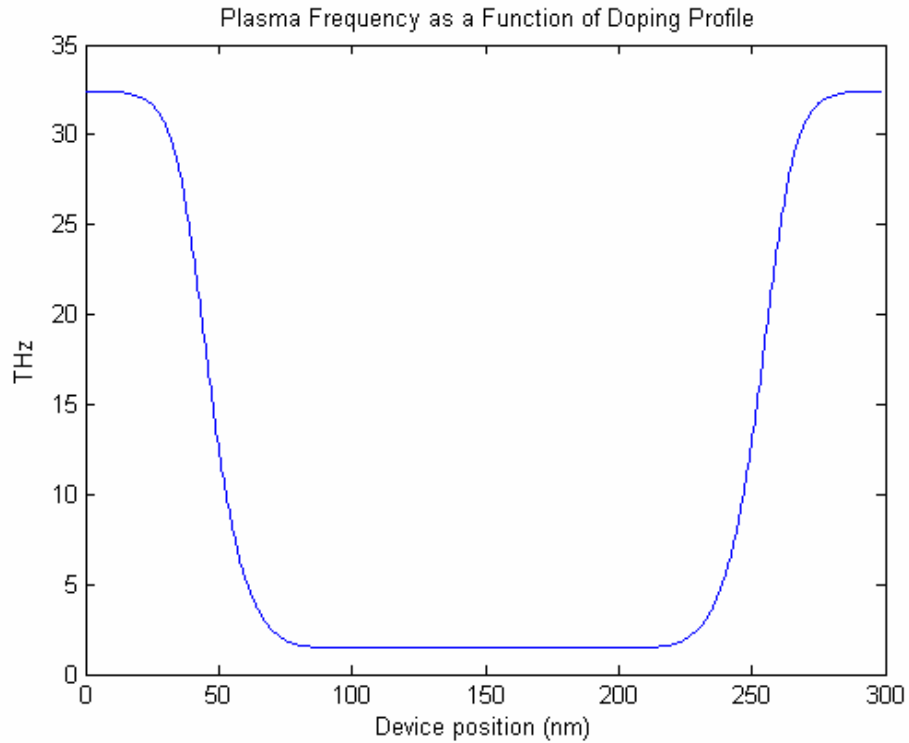


Figure 6: Plasma Frequency Ballistic Diode vs. Doping Profile

The general equations used in the model developed to simulate the benchmark diode are shown below. Equations (68-71) are used for the semiconductor model and equations (72-73) are used for the FDTD-EM grid. The semiconductor device is assumed to be sufficiently small, thus it may be embedded into a single cell of the FDTD-EM grid as a 2-port device discussed in the following section.

Semiconductor Model: Balance Equation Model
Conservation of Mass

$$\frac{\partial n}{\partial t} = -\nabla \cdot (\vec{v}_d n) + \left(\frac{\partial n}{\partial t} \right)_c \quad (68)$$

Conservation of Momentum

$$\frac{\partial(n\vec{p})}{\partial t} = -\nabla \cdot (n\vec{v}_d \vec{p}_d) + en\vec{F} - \nabla(nk_B T) + \left(\frac{\partial(n\vec{p})}{\partial t} \right)_c \quad (69)$$

Conservation of Energy

$$\frac{\partial(nw)}{\partial t} = -\nabla \cdot (n\vec{v}_d w + \vec{v}_d nk_B T - \kappa \nabla T) + e\vec{F} \cdot \vec{v}_d n + \left(\frac{\partial(nw)}{\partial t} \right)_c \quad (70)$$

Electrostatic Effects: Poisson's Equation

$$\nabla \cdot \vec{E} = \frac{1}{\epsilon_o} \rho_c \quad (71)$$

FDTD-EM: Maxwell's curl equations (non-dispersive)

$$\nabla \times \vec{B} - \frac{1}{c^2} \frac{\partial \vec{E}}{\partial t} = \mu_o \vec{J} \quad (72)$$

$$\nabla \times \vec{E} + \frac{\partial \vec{B}}{\partial t} = 0 \quad (73)$$

CHAPTER 5: MODEL COUPLING METHODOLOGY

This work seeks to couple an FDTD-EM simulator with an HDM model in a computationally efficient manner. The basic goal is to extend El-Ghazaly's approach by removing the unified grid architecture and significantly reducing the computational overhead. A novel technique that extends Picket-May's method for embedding SPICE structures into the FDTD-EM grid through including HDM models is also tested [8]. The method identifies the effective means of transferring the energy between the two models at specific input and output ports, effectively eliminating the spatial grid co-location requirement, thus making splitting of the time-stepping less challenging. To benchmark this new methodology the generally accepted test structure of the $n-i-n$ ballistic diode was used. The diode is a "voltage-driven current" device making natural the application of the Thevenin equivalent circuit method proposed by Picket-May [8].

Previous sections dealt with the HDM review, development, and recent advances. Simply using those results to achieve a stable convergent HDM simulator is a non-trivial task. To evaluate the coupling methodology, three separate models were implemented each with different discretization methods. The Lax-Wendroff method proposed by Tomizawa, the weighted upwind method described by Aste & Vahldieck, and a novel leapfrog method, that is proposed in this thesis for the first time and is second-order accurate in time and space without the numerical dispersion associated with the upwind method, while including the pressure tensor that Tomizawa's method omitted. Additionally, three different excitation methods were tested for the three models. This work further expands on the previous work published by the same author [4].

5.1 Physical System Coupling Method

The systems under investigation describe two disparate systems. The electromagnetic simulator (EMS) describes 3D electromagnetic wave propagation, while the device simulator (DS) describes the effects of ensemble charged particle motion. Embedding passive devices into FDTD-EM grids is well known and understood [8]. Picket-May presented a generic approach to embed complex non-linear devices into the FDTD-EM grid, by embedding SPICE simulation results into the grid. The complex SPICE-derived models were coupled to FDTD-EM grid by coupling the energy using Thevenin equivalent and Norton equivalent circuits.

5.1.1 Picket-May Model Coupling (FDTD-EM & SPICE)

Picket-May introduced an effective method to embed time-domain SPICE models into the FDTD-EM grid space. The next several sections contain a summary of the method presented in [8] with interfacing expansions to meet the requirements of the HDM model. The methodology used is similar; however, the FDTD-EM lattice inductance or capacitance effects are omitted in the excitation of the HDM model for each time-step. Mitigation of the omission of the lattice effects is done with local variable gridding of the FDTD-EM lattice, and is discussed in section 5.1.4. The Picket-May method incorporates the FDTD-EM lattice impedance effects directly with the SPICE engine. A simpler method to help mitigate these effects is examined in this section. Several methods for interpolating excitation methods are also examined in the results section.

5.1.2 Thevenin Equivalent Model

The FDTD-EM grid space is based upon the Yee staggered grid in time and space using the Leapfrog discretization in 3D Cartesian space [6,37]. FDTD-EM tools provide full

vector E - and H - field distributions in time and space. To correlate these field distributions to the usual circuit quantities of voltage and current the following fundamental expressions (74, 75) can be used:

$$V(t, x_i) = \int_{C_V} \vec{E}(t, x_i) \cdot d\vec{l} \quad (74)$$

$$I(t, x_i) = \oint_{C_i} \vec{H}(t, x_i) \cdot d\vec{l} \quad (75)$$

C_V : contour from a ground to the circuit location

C_i : closed loop containing the conductor

5.1.3 Thevenin Equivalent circuit “Looking into” the FDTD lattice

The model used to evaluate the proposed coupling method is the Thevenin equivalent circuit (“voltage-driven current” device). The complementary approach for the Norton equivalent (“current-driven voltage” source) model is equally valid and presented in [8]. Figure 7 shows the Thevenin equivalent looking into the FDTD grid from the device, forming the basis for the coupling method. Equation (76) shows the equivalent circuit model, that includes both the device effects $V_{dev}[I_{dev}(t)]$ and the lattice effects $L_\theta \frac{dI_{dev}(t)}{dt}$.

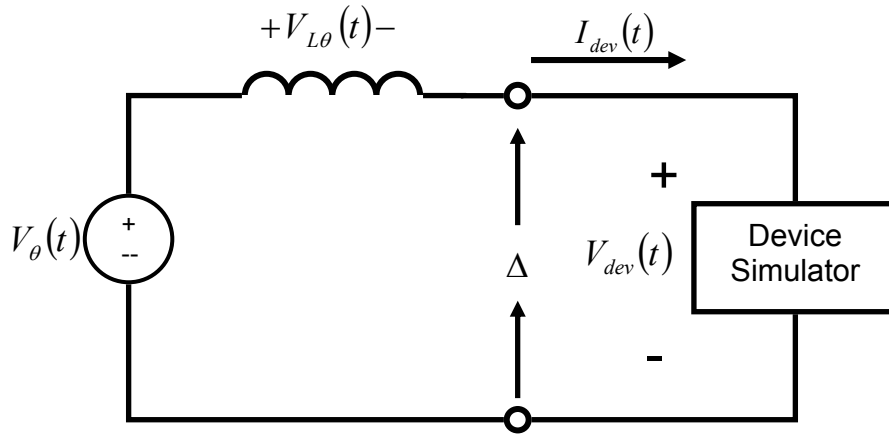


Figure 7: Thevenin Equivalent circuit for FDTD-EMS, DS coupling

$$V_{\theta}(t) = L_{\theta} \frac{dI_{dev}(t)}{dt} + V_{dev}[I_{dev}(t)] \quad (76)$$

$V_{dev}[I_{dev}(t)]$: The highly non-linear voltage-current characteristic of the HDM model

$L_{\theta} \frac{dI_{dev}(t)}{dt}$: FDTD-EM Lattice effects

Equations (77) and (78) provide the voltage source for the Thevenin equivalent circuit in Figure 7. By including the 4 equivalent voltage loops as shown in Figure 8, some of the effects of non-TEM modes are mitigated if the feeding structure to the device under test is a non-TEM type, according to Taflove [8].

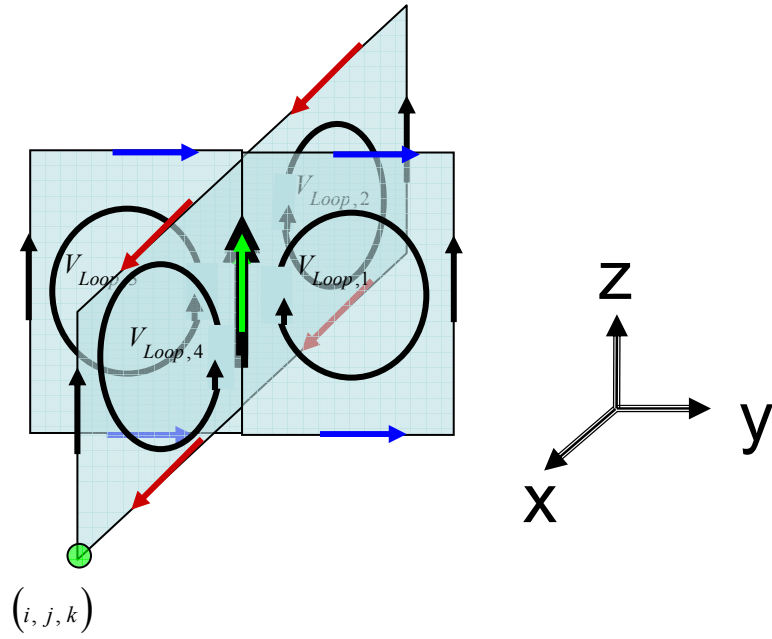


Figure 8: Thevenin Equivalent Voltage Loops

$$V_{\theta} = \frac{1}{4} \sum_{i=1}^4 V_{loop,i}(t) \quad (77)$$

$$V_{loop,i} = -\oint_{\Gamma_i} \vec{E} \cdot d\vec{\Gamma}_i \quad (78)$$

Equation (76) includes both the voltage current characteristics of the device model and the FDTD-EM lattice effects. Picket-May's technique has the advantage of directly implement the lattice effects within SPICE. Directly incorporating the lattice effects into the HDM model would require a significantly more complex solution, to an already challenging problem, alternate methods are explored in the next section. The current response of the SPICE engine or HDM model is coupled back into the FDTD-EM lattice via (79).

$$\nabla \times \vec{H} = \vec{J}_{lattice} + \frac{\partial D}{\partial t} + \vec{J}_{dev} \quad 4 \quad (79)$$

\vec{J}_{dev} : Device response current density term.

$\vec{J}_{Lattice}$: FDTD-EM Lattice current density term.]

5.1.4 Lattice Impedance

The equivalent circuit model shown in Figure 7, includes the lattice inductance which is a part of the SPICE model in Picket-May's approach. As the HDM has no spice engine, the effect of the inductance needs to be examined in terms of the numerical effects due to a potential replacement or omission. The inductance of FDTD-EM lattice is given by the relations in (80) and (81).

$$\Delta = \frac{\lambda_{min}}{N_{\lambda}} ; \text{Typically } \Delta x = \Delta y = \Delta z \quad (80)$$

$$L_{lattice} = \frac{\mu_o \Delta}{4} = L_{\theta} \quad (81)$$

By looking at Figure 7, it is can be easily observed that the inductance for the Thevenin equivalent or capacitance for the Norton equivalent, in general, provides an exponential smoothing of the excitation, expressed in the typical expressions for an RL circuit are shown in (82) and (83).

$$\tau = L_{lattice} / R_{load} \quad (82)$$

$$V_{dev}(t) = V_{\theta} (1 - e^{-t/\tau}) \quad (83)$$

RL response characteristic

Equations (82) and (83) can be used to estimate the Voltage at the present device terminal. For example, Figure 9 and Figure 10 show the voltage response curves of

⁴ $\vec{J}_{lattice}$ is considered small and often omitted final formulations

equation (83) for various constant resistive loads for two different FDTD-EM spatial cell sizing. Figure 10 shows the effect of reducing the FDTD-EM cell size, by a factor of 10, and their effect on the voltage applied to the device through the Thevenin equivalent circuit for a specific implementation, where the maximum frequency of interest is $f_{\max} = 10\text{GHz}$, and the time step and space step are calculated using $\Delta x = \lambda_{\min}/20$, $\Delta t_{EMS} = 1/20 f_{\max}$. The time-axis is a single FDTD-EM time step.

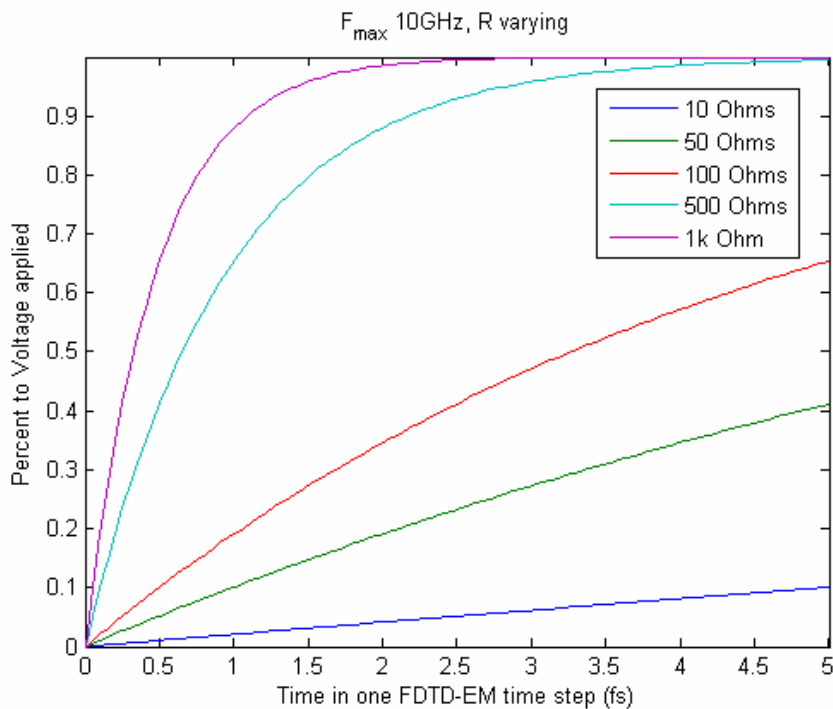


Figure 9: V-Thevenin Smoothing

Figure 10 shows the effect of reducing the FDTD-EM cell size by a factor of 10 on the lattice impedance with the same time step. The FDTD-EM lattice impedance is highly dependent on the cell size as the difference. Reducing the cell size by a factor of 10 (from 5 to 0.5) shows significant improvement in response time, Figure 9. Practically, this reduction can be easily accomplished using local variable gridding near HDM embedding point without significantly impacting the performance of the FDTD-EM

simulator. Also, the effective time constant of the device can be monitored during simulation to ensure 99.5% of the excited voltage is obtained. It is well understood that RL and RC time constant rise and decay times reach 99.5% of the terminal value at 5τ , by post processing the effective time constant compliance can be assured. Figure 10 provides an example.

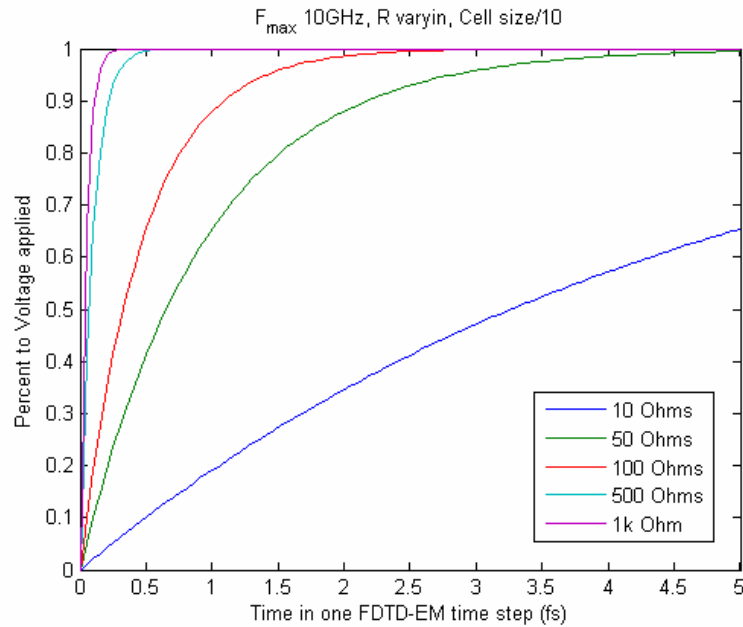


Figure 10: V-Thevenin Response for $\Delta x_{EMS} / 10$

5.1.5 Coupling the Models in Time

The methods for calculating the voltage excitation from the FDTD-EM lattice and deriving the current response of the device have been effectively identified, leaving the time evolution to be determined. The leapfrog method used in the FDTD-EM offsets the E-field & H-field one-half step in time and space. The voltage excitation is calculated from the E fields at time $(t = t_0)$. This time-updated voltage value is applied to the device

model for a full time step that covers from $\left(t = t_0 - \frac{1}{2} \Delta t\right)$ to $\left(t = t_0 + \frac{1}{2} \Delta t\right)$ as the E-fields are considered constant in the FDTD-EM grid throughout the whole time-step. The resultant HDM-calculated current is applied back to the FDTD-EM grid in terms of an effective current density at $\left(t = t_0 + \frac{1}{2} \Delta t\right)$. Equations (84) through (87) show the process as they relate the two systems. The method allows for the two systems' time steps to vary independently effectively removing the time discretization limitation on the coupled models.

The new excitation voltage is applied at time step (t_0) from the calculated

$$V|_{i,j,k}^{t_0} = \vec{E}_z|_{i,j,k}^{t_0} \Delta z \quad (84)$$

Current response is transformed to current density

$$\vec{J}_{\hat{z}}(t_0 + \Delta t / 2)_{dev} = \frac{I_{dev}(t_0 + \Delta t / 2)}{\Delta x \Delta y} \quad (85)$$

Current density response is fed back into the system

$$\frac{\vec{E}_z|_{i,j,k}^{t_0+\Delta t} - \vec{E}_z|_{i,j,k}^{t_0}}{\Delta t} = \frac{1}{\epsilon} \left(\nabla \times \vec{H}_{i,j,k}^{t_0+\Delta t/2} - \vec{J}_{\hat{z},dev}|_{i,j,k}^{t_0+\Delta t/2} \right) \quad (86)$$

The new excitation voltage is applied and the cycle is repeated

$$V|_{i,j,k}^{t_0+\Delta t} = \vec{E}_z|_{i,j,k}^{t_0+\Delta t} \Delta z \quad (87)$$

5.1.6 Coupling the models in the FDTD-EM grid

The new method treats the HDM a port defined device. The excitation voltage calculated via the closed loop integral defined by (77) and (78). The current density response is

calculated using (86). It is important to note the HDM is assumed to be embedded into a single FDTD-EM cell and assumed to be aligned the along the +z axis. Positive current flow is assumed to flow in the +z direction for proper integration into the FDTD-EM grid. The device has two ports (Source and Drain). As the device is symmetric, the ports are a matter of definition. For the tests conducted, the Source was considered to be at x=0 of the HDM model, and the Drain at the end of the device. The drain was grounded in all tests performed and the ground was treated as perfect ground, sinking and sourcing carriers as required. The Source was the interface for both the input and output.

5.1.7 Voltage Excitation Method

Reducing the FDTD-EM cell sizing should reduce the Lattice effects on the excitation and response characteristics of the embedded FDTD-HDM device. Moving forward with that assumption examining the method for discretization of the excitation from the FDTD-EM lattice can be examined. The FDTD-EM lattice provides two values: the voltage $V|_{i,j,k}^{t_0-\Delta t}$ at the device port from the previous time step and the voltage $V|_{i,j,k}^{t_0+\Delta t}$ at the current time step current time step. Without retaining further information and using advanced prediction techniques only two real methods of discretization are possible. The simplest method is to apply a piecewise-step approximation based only on the current FDTD-EM time step applied voltage. A better method would be a piecewise linear approximation in which the previous time step voltage was known and could be linearly interpolated, as shown in equation (88). Both of these approaches are to be compared in the results section.

$$V|_{i,j,k}^{t_{HDM}} = V|_{i,j,k}^{t_0-\Delta t} + \left(\frac{\left(V|_{i,j,k}^{t_0+\Delta t} - V|_{i,j,k}^{t_0-\Delta t} \right)}{\Delta t_{EMS}} \right) \left(t_{HDM} \Delta t_{HDM} - t_{0,EMS} \Delta t_{EMS} \right) \quad (88)$$

5.1.8 Current Response

The current response that is fed back into the system is different between the SPICE and the HDM tools. The SPICE model directly returns the value of the current whereas the HDM returns the current density at the output port of the device. Coupling the current response of the two models is relatively straight forward. The current response of the SPICE is transformed into current density via (89), assuming that the xy-cross-section of the device covers 1 FDTD-EM cell to both x- and y- directions.

$$\vec{J}_{\hat{z}}(t)_{dev} = \frac{I_{dev}(t)}{\Delta x \Delta y} \quad (89)$$

The HDM tool returns the current density at the port of the device, and therefore must be transformed from current density of the device port to total output current, then finally to current density of the FDTD-EM lattice for the device using (90) – (93).

$$\vec{J}_{HDM} = -qn\vec{v} \quad (90)$$

$$\vec{I}_{Dev} = (\vec{J}_{HDM})(\text{Device Terminal Area}) \quad (91)$$

$$\vec{J}_{\hat{z}}(t)_{dev} = \frac{I_{dev}(t)}{\Delta x \Delta y} \quad (92)$$

The result of (92) is fed back into the FDTD-EM lattice using

$$\frac{\vec{E}_z \Big|_{i,j,k}^{t_0+\Delta t} - \vec{E}_z \Big|_{i,j,k}^{t_0}}{\Delta t} = \frac{1}{\epsilon} \left(\nabla \times \vec{H}_{i,j,k}^{t_0+\Delta t/2} - \vec{J}_{\hat{z},Dev} \Big|_{i,j,k}^{t_0+\Delta t/2} \right) \quad (93)$$

The literature is unclear on whether a hard or soft source is used at the response point of the FDTD-EM grid for the Picket-May method. Taflove examined the errors associated with hard sources in 1, 2 and 3 dimensions. He found significant errors were propagated

only in the 1D case. The errors generated in 2D and 3D were small as the percentage of reflected wave interacting with the hard source was extremely small [37].

CHAPTER 6: HDM MODEL

The hereby implemented hydrodynamic model is similar to models used by Aste & Vahldieck, and El-Ghazaly as it includes the diffusion effects caused by the very large concentration gradients with one major departure. The new method uses a leapfrog method in time and space, not just space. This makes the model significantly more stable and second order in time and space for all variables. In previous sections, both the Aste & Vahldieck and El-Ghazaly methods were evaluated; this section details the new and novel model being evaluated in this work. The complete model to be discretized is presented below. To re-iterate the complexity of the hydrodynamic model, the final form of the system of equations is highly dependent upon the assumptions used to simplify the general model. The following is a list of the assumptions used to create the new HDM model.

Assumptions and Simplifications

- Carrier Concentration variation in time is trivial
 - Simplified Conservation of Momentum
 - Simplified Conservation of Energy
- Electron effective mass fixed or varied based on static assumption
- Carrier Concentration Gradient is non-trivial in space
- System can be partially decoupled in space and time
 - Scalars at nodal points
 - Vectors at $\frac{1}{2}$ nodal points
- Carrier Relaxation times can be approximated using BW model
- Heat flux is approximated by Fourier's law
 - Heat flow is approximated by Franz-Wiedemann Law
 - No significant heat flows from Gas to Lattice
- Semiconductor type is "Silicon"-like
 - A single spherical band sufficiently simulates bands
 - No Conservation of Mass Collision terms
 - Recombination and Generation of carriers insignificant
 - No additional Conservation of Mass Collision Terms
- No transverse EM waves propagating

- Maxwell's Curl Equations for dispersive media omitted
- Poisson Equation – Electrostatic oscillations only (Plasma waves)
- Magnetic field interaction is small and can be omitted
- Simulation is only being tested in the sub-supersonic regions
 - Shock wave capturing not required
- 1D model
 - Pressure Tensor term in Conservation of momentum simplified to 1D

6.1.1 Model Development and Simplification

In their most generic form, the conservation of momentum and energy equations contain

particle density values in the time derivative $\frac{\partial(n\vec{p})}{\partial t}$ $\frac{\partial(nw)}{\partial t}$ that is impractical to solve for

numerically and must be isolated. If the carrier concentration is assumed to be fixed in time, then “n” becomes a scalar and can be factored out. The carrier momentum can be converted to velocity, in the same method, transforming the time derivative terms into (94) and (95). This simplification is valid for the following cases.

- time variations in the carrier concentrations are small
- grid is staggered such that over the complete HDM time step the concentration is actually held constant
- time variations in carrier effective mass are small, typically fixed in model assumptions

$$\frac{\partial(n\vec{p})}{\partial t} \Rightarrow nm^* \frac{\partial\vec{v}_d}{\partial t} \quad (94)$$

$$\frac{\partial(nw)}{\partial t} \Rightarrow n \frac{\partial w}{\partial t} \quad (95)$$

Conservation of Mass

$$\frac{\partial n}{\partial t} = -\nabla \cdot (\vec{v}_d n) + \left(\frac{\partial n}{\partial t} \right)_C \quad (96)$$

Conservation of Momentum

$$nm^* \frac{\partial\vec{v}_d}{\partial t} = -\nabla \cdot (n\vec{v}_d \vec{p}_d) + en\vec{F} - \nabla(nk_B T) + \left(\frac{\partial(n\vec{p})}{\partial t} \right)_C \quad (97)$$

Conservation of Energy

$$n \frac{\partial w}{\partial t} = -\nabla \cdot (n\vec{v}_d w + \vec{v}_d n k_B T - \kappa \nabla T) + e\vec{F} \cdot \vec{v}_d n + \left(\frac{\partial(nw)}{\partial t} \right)_c \quad (98)$$

Wiedemann–Franz law

$$\kappa = \frac{5k_B n T}{2m^* v_p(w)} \quad (99)$$

Poisson's Equation

$$\frac{\nabla^2 \phi}{\partial x^2} = \frac{q}{\epsilon_o \epsilon_r} (N_D - n_i) \quad (100)$$

Momentum Relaxation Time

$$\tau_p = \frac{m}{e} \mu_0 \frac{T_0}{T} \quad (101)$$

Energy Relaxation time

$$\tau_w = \frac{m}{e} \mu_0 \frac{T_0}{T} + \frac{3}{2} \frac{k_B}{e v_s^2} \mu_0 \frac{T T_0}{T + T_0} \quad (102)$$

Momentum Relaxation Rate

$$v_p(w) = \tau_p \quad (103)$$

Substituting the collision terms for the Baccarani- Wordeman model [25] leads to the following modified set of equations:

Conservation of Momentum

$$nm^* \frac{\partial \vec{v}_d}{\partial t} = -\nabla \cdot (n\vec{v}_d \vec{p}_d) + en\vec{F} - \nabla(nk_B T) + \frac{nm^* \vec{v}_d}{\tau_p} \quad (104)$$

Conservation of Energy

$$n \frac{\partial w}{\partial t} = -\nabla \cdot (n\vec{v}_d w + \vec{v}_d n k_B T - \kappa \nabla T) + e\vec{F} \cdot \vec{v}_d n + \frac{n(w - w_o)}{\tau_w} \quad (105)$$

Total Energy Relation

$$T = \frac{2}{3k_B n} \left(nw - \frac{1}{2} nm v_d^2 \right) \quad (106)$$

Implemented HDM Model Equations for the proposed HDM simulator

$$\frac{\partial n}{\partial t} = -\vec{v}_d \cdot (\nabla n) - n \nabla \cdot (\vec{v}_d) \quad (107)$$

$$\frac{\partial \vec{v}_d}{\partial t} = -\frac{1}{nm^*} \nabla \cdot (n \vec{v}_d \vec{p}_d) + \frac{e\vec{F}}{m^*} - \frac{1}{nm^*} \nabla (nk_B T) + \frac{\vec{v}_d}{\tau_p} \quad (108)$$

$$\begin{aligned} \frac{\partial w}{\partial t} = & -\frac{1}{n} \nabla \cdot (n \vec{v}_d w) - \frac{1}{n} \nabla \cdot (\vec{v}_d nk_B T) \\ & - \frac{1}{n} \nabla \cdot \left(-\frac{5k_B n T}{2m^* v_p(w)} \nabla T \right) + e\vec{F} \cdot \vec{v}_d + \frac{(w - w_o)}{\tau_w} \end{aligned} \quad (109)$$

$$\frac{\nabla^2 \varphi}{\partial x^2} = \frac{q}{\epsilon_o \epsilon_r} (N_D - n_i) \quad (110)$$

These four equations (107)-(110) have been discretized and form the core equations of the HDM model under consideration. Four variables, carrier concentration (n), average carrier velocity (\vec{v}_d), average carrier energy (w), and electric potential(φ) have been solved for three scalars (n, w, φ) and one vector (\vec{v}_d) as independent variables. The static E-field is a dependent variable based on the solution of the Poisson equation. The total electron energy (T_e) is also a dependent variable and is calculated from the independent variables. The relaxation times are calculated in closed form according to the Baccarani-Wordemann model.

6.2 Discretization

6.2.1 Gridding Methodology

The HDM is a highly-coupled non-linear system. In previously published approaches, discretization has been accomplished by either staggering the vectors and scalars at full and half nodal points or setting all variables at the nodal points at the same time step. Then, advanced discretization techniques are typically used in time. The assumption that the equations cannot be sufficiently decoupled to stagger them in time produces a 1st order in time approximation and a second-order in space that several authors have tried to correct in order to enhance the numerical stability. Tomizawa used a Crank-Nicolson semi-implicit method, Aste & Vahldieck used a weighted upwind scheme, and El-Ghazaly used a hybrid method that included both a standard upwind method and a Lax-Wendroff method.

The novel method proposed here is to extend the basic tenets of Yee's Leapfrog method in space and time Maxwell's Curl equation discretization to the HDM. If one accepts that the equations can be sufficiently decoupled to stagger the gridding in space [1,2,24], the staggering those variables in time is the next natural extension. The developed simulator staggers the scalar variables (n, w, m^*, φ) on the full nodal points of the grid and the vector variables (\vec{v}_a, \vec{E}) on the half nodal points of the HDM grid in time and space as seen in Figure 11 [38].

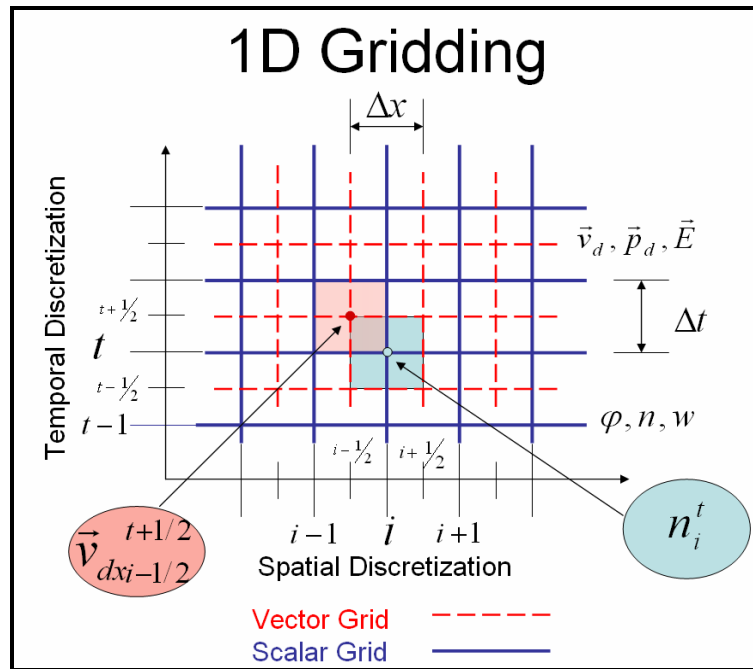


Figure 11: Gridding Method

6.2.2 Discretization

The discretization of the equations (107)-(110) is a natural extension of the grid shown in Figure 11. For simplicity only the discretization of the conservation of mass equation is displayed, since the rest of the equations can get similarly discretized. The method is slightly more complicated than the Yee method for Maxwell's curl equations [39]. Commonly, the grid is staggered using vector or scalar as the discerning criterion. The complication occurs in that each of the equations contains both scalars and vectors on the right hand side of the equation (spatial portion). As is seen in the following discretization, the carrier concentration lies on a nodal point, but the leapfrog central discretization scheme calls for the scalar values at the $\frac{1}{2}$ node point. This requires the scalar value to be averaged with the nearest neighbors. The vector quantities lie on their "natural" points and can be used directly. The conservation of mass is fully discretized with the averaging values back-substituted into the final discretization to show the

symmetric nature of the averaging (116). The Aste & Vahldieck weighted upwind discretization methodology produces un-intended asymmetry in the discretization that affects the stability and convergence of the model.

Discretization of the Conservation of Mass equation

$$\frac{\partial n}{\partial t} = -\nabla \cdot (\vec{v}_d n) \quad (111)$$

Discretize for the nodal (i^{th} -point)

$$n_i^{k+1} = n_i^k + \Delta t \left(-\nabla \cdot (\vec{v}_d n) \Big|_i^k \right) \quad (112)$$

Expand the right hand side

$$-\nabla \cdot (\vec{v}_d n) \Big|_i^k = -\frac{\left(n \Big|_{i+1/2}^k v_{dx} \Big|_{i+1/2}^{k-1/2} - n \Big|_{i-1/2}^k v_{dx} \Big|_{i-1/2}^{k-1/2} \right)}{\Delta x} \quad (113)$$

An example of averaging a scalar for a nodal point

$$n \Big|_{i+1/2}^k = \frac{\left(n \Big|_i^k + n \Big|_{i+1}^k \right)}{2} \quad (114)$$

Substitute in the average values as required and the final form effectively becomes

$$-\nabla \cdot (\vec{v}_d n) \Big|_i^k = \frac{\left(n \Big|_{i+1}^k v_{dx} \Big|_{i+1/2}^{k-1/2} + n \Big|_i^k v_{dx} \Big|_{i+1/2}^{k-1/2} - n \Big|_i^k v_{dx} \Big|_{i-1/2}^{k-1/2} - n \Big|_{i-1}^k v_{dx} \Big|_{i-1/2}^{k-1/2} \right)}{2\Delta x} \quad (115)$$

This equation is substituted back into the original i^{th} point discretization

$$n_i^{k+1} = n_i^k + \Delta t \left(-\frac{\left(n \Big|_{i+1}^k v_{dx} \Big|_{i+1/2}^{k-1/2} + n \Big|_i^k v_{dx} \Big|_{i+1/2}^{k-1/2} - n \Big|_i^k v_{dx} \Big|_{i-1/2}^{k-1/2} - n \Big|_{i-1}^k v_{dx} \Big|_{i-1/2}^{k-1/2} \right)}{2\Delta x} \right) \quad (116)$$

6.2.3 Space and Time Step Disparity

After the FDTD-EM and HDM systems have been discretized and methods for their coupling have been presented, the spatial and temporal disparity between the two systems is the final problem to be reckoned. The FDTD-EM tool space and time steps are determined by the maximum frequency of interest. For a typical leading edge RF device ($f_{\max} = 200\text{GHz}$) the time step is on the order of 10^{-13} seconds, and the spatial step on the order of 10^{-4} meters. The FDTD-HDM tool space and time steps are predominantly determined by the doping profile of the device. For the benchmark device used within this work, the spatial cell sizing is on the order of 10^{-10} meters, and the time step is on the order of 10^{-18} seconds. This represents a disparity of 5 orders of magnitude in time and 6 orders of magnitude in space between the models. Coupling of these systems requires dealing with both of these issues. The discretization and port definitions let the HDM be a separate embedded device in the grid interacting with FDTD-EM only via the defined input and output ports; this makes the spatial cell sizing a trivial case. The time stepping presents a more difficult problem. The approach to solving this issue is presented in the next section. Eliminating the unified spatial and temporal grid represents computational savings 10 orders of magnitude per time step and space step of the FDTD-EM grid being co-simulated.

6.2.4 Excitation Methodology

The excitation is implemented via the applied voltage at the ports. Several methods were tested. One method requires only the current FDTD-EM voltage (step excitation), the other method requires knowledge of the previous time step voltage to perform linear

interpolation. The methods tested were used on all previously developed models (Lax-Wendroff, A&V Upwind, and Leapfrog).

- **Smooth – HDM:** The excitation function is discretized for each HDM time step in a piecewise step approximation. The time stepping is very small and as such has a very smooth approximation
- **Step – EM:** Step wise excitation based on the current FDTD-EM calculated applied voltage. The voltage is applied in with a step function and held constant for each EMS-dt.
- **Linear – EM:** Piecewise linear approximation of the Voltage from the previous FDTD-EM step and the current FDTD-EM time step discretized to the FDTD-EM time step.

Figure 12 shows the graphical representation of these excitation methods. The standard excitation methodology is to use a known stable zero bias condition as the initial condition for the device under test. The simulator runs with a zero bias condition to ensure steady state, then the bias voltage is ramped from 0V to 1VDC. The DC bias is held constant to allow the device to stabilize. Then, a pure sinusoid is summed with the DC bias. Discretization of the excitation signal will be performed utilizing each of the three previously described methods for each of the HDM models under investigation to couple with the FDTD-EM grid.

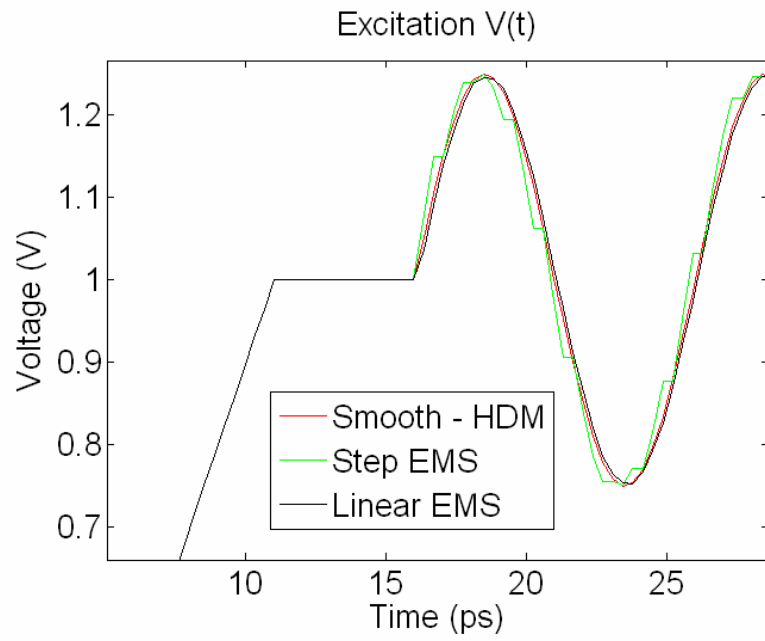


Figure 12: Excitation Methodology

CHAPTER 7: RESULTS

The previous sections have described the different models used, the discretization approaches, and the methods used to couple and excite them to illicit a response. This section will detail the results of this work. The HDM model developed is a single-carrier type 1D tool. The base model is generic for single-carrier type devices (N-MOS, P-MOS). As such, the proper test structure needed to be identified. The generally accepted benchmark case is an *n-i-n* ballistic diode [1, 2, 5, 24]. In recent years, Aste & Vahldieck have published several papers with a submicron ballistic diode well documented in terms of critical variables and results. The benchmark diode tested with results presented is nearly identical to the Aste & Vahldieck structure published for easy comparison

Two main topics are under investigation in this work, a new HDM discretization and a new and novel method to couple the FDTD-EM and FDTD-HDM simulators. Both topics need to be examined in terms of accuracy/validity and computational improvements. The benchmark ballistic diode is used to evaluate the basic functionality of the HDM tool and consistency with previously published results. The other topic of interest is coupling the disparate systems. Three excitation methods are applied to the Aste & Vahldieck Upwind HDM method and the new Leapfrog HDM method. The Lax-Wendroff method is unsuitable for the benchmark device under consideration and was dropped for further testing in the AC section. The results for all three models showing are presented in the DC section.

7.1 Benchmark Diode

The benchmark case typically used for the evaluation of any HDM model is a Silicon n-i-n (“ballistic”) diode, which forms the basic building block for many MOS devices. The numerical device presented here is a slightly elongated ballistic diode with the same gross doping characteristics presented in [24,30]. The Aste & Vahldieck publications failed to describe the doping profiles adequately for reproduction, The doping profile is an exponential taper as previously published by Tomizawa [1]. A complete list of significant device characteristics is listed below Figure 13 showing the doping profile for the benchmark device. Aste & Vahldieck’s effective mass was used even though it represents the minimum effective mass along the axis of the device’s wave function solution; thereby overestimating the transit speeds by reducing the carrier inertia. The underestimation of the carrier effective mass makes a stable solution more challenging. Nevertheless, the transition width was adjusted such that all models were stable and relatively convergent. The other established method for finding the carrier effective mass is to use El-Ghazaly’s position dependent carrier effective mass; however, this would require re-formulation of the equations to include the spatial derivatives of the variable carrier effective mass[2].

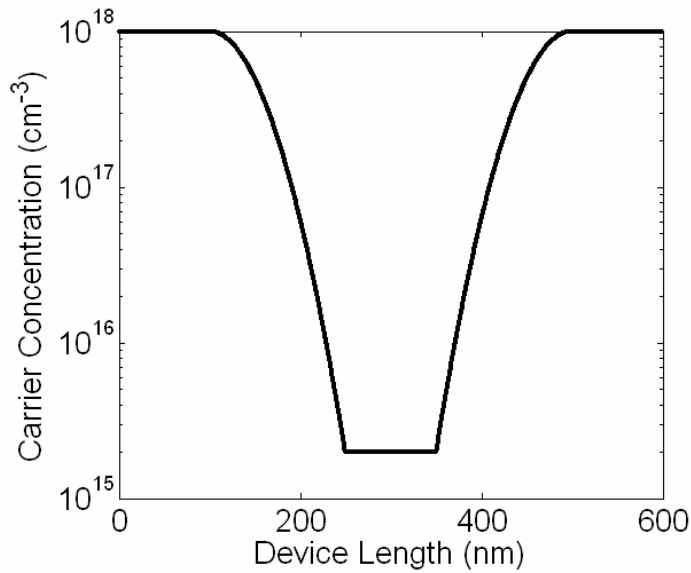


Figure 13: Doping Profile

Key Benchmark Device Characteristics

- Drain: length: 0.20um doping: $ND=10^{18} \text{ cm}^{-3}$
- Source: length: 0.20um doping: $ND=10^{18} \text{ cm}^{-3}$
- Channel: length: 0.15um doping: $ND=10^{18} \text{ cm}^{-3}$
- Temperature of Lattice: 300K
- Electron effective mass: $(0.26 \cdot \text{mass electron at rest})$,
- Saturation velocity: $1.03 \times 10^5 \text{ m/s}$
- Applied DC bias = 1.0V

7.2 Initial Conditions

All used models are susceptible to bad initial conditions to varying degrees. Without proper initial conditions, the most important being a reasonable carrier distribution, the model diverges rapidly. No text suggests valid initial conditions for the simulator, merely stating that great care must be taken. As such, the author was forced to use the brute force method of trial and error to achieve stability and convergence. The determining factor for both the Lax-Wendroff and Leapfrog method is shown in Figure 14 and

equation (117). When the diffusive force is equal to the force from the built-in potential, the device is in steady state. The A&V upwind method is similar, but never converges to a steady state where the average carrier velocity is near zero for the entire device. This is a numerical artifact of the initial conditions, as the upwind was meant to capture near supersonic flows not stationary. As the average velocity increases the solution does converge for most cases. If the initial condition is too far off the system will stabilize, but not converge as seen in Figure 18 . This odd behavior is a function of the asymmetric nature of the A&V upwind discretization, not the HDM model. Figure 15 shows the resultant carrier distribution as it varies from the doping profile for all three models. Figure 16 shows a comparison between the average carrier velocities for the three methods at “rest.” The “rest” condition is the device in the off state with no excitation and the model has reasonably stabilized. Results from the rest cases are shown in Figure 14, Figure 15, and Figure 16. The initial conditions for Leapfrog and Lax-Wendroff methods were nearly identical and very near zero. The A&V Upwind method varied as expected for the no bias case.

$$en\vec{F} = \nabla(nk_B T) \quad (117)$$

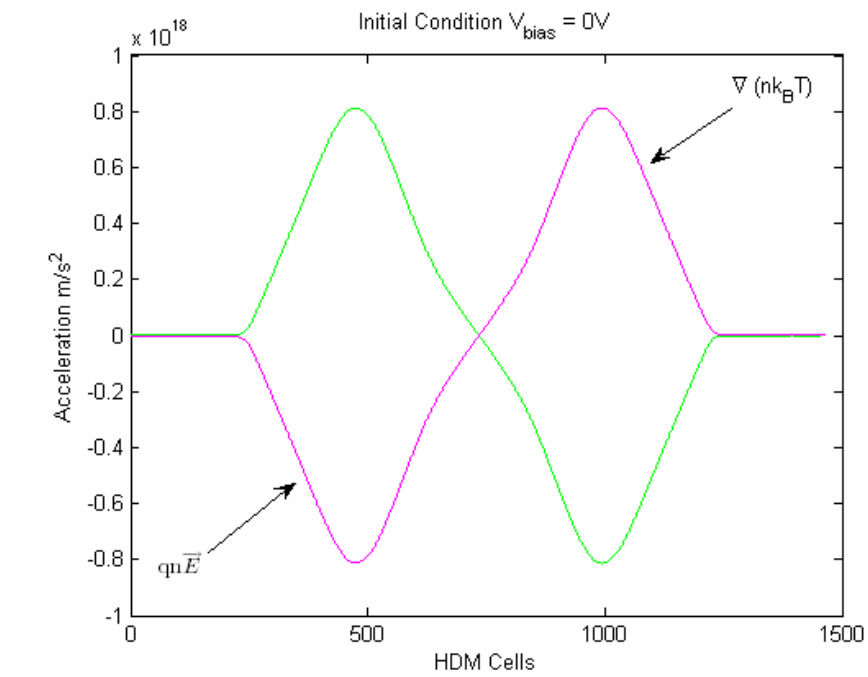


Figure 14: Initial Condition for Lax-Wendroff and Leapfrog

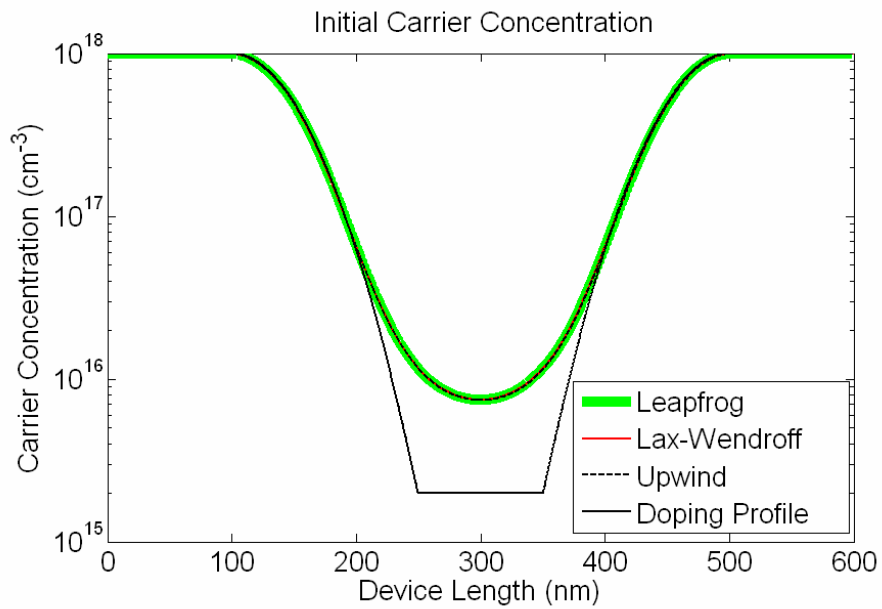


Figure 15: Initial Carrier distribution for Lax-Wendroff and Leapfrog

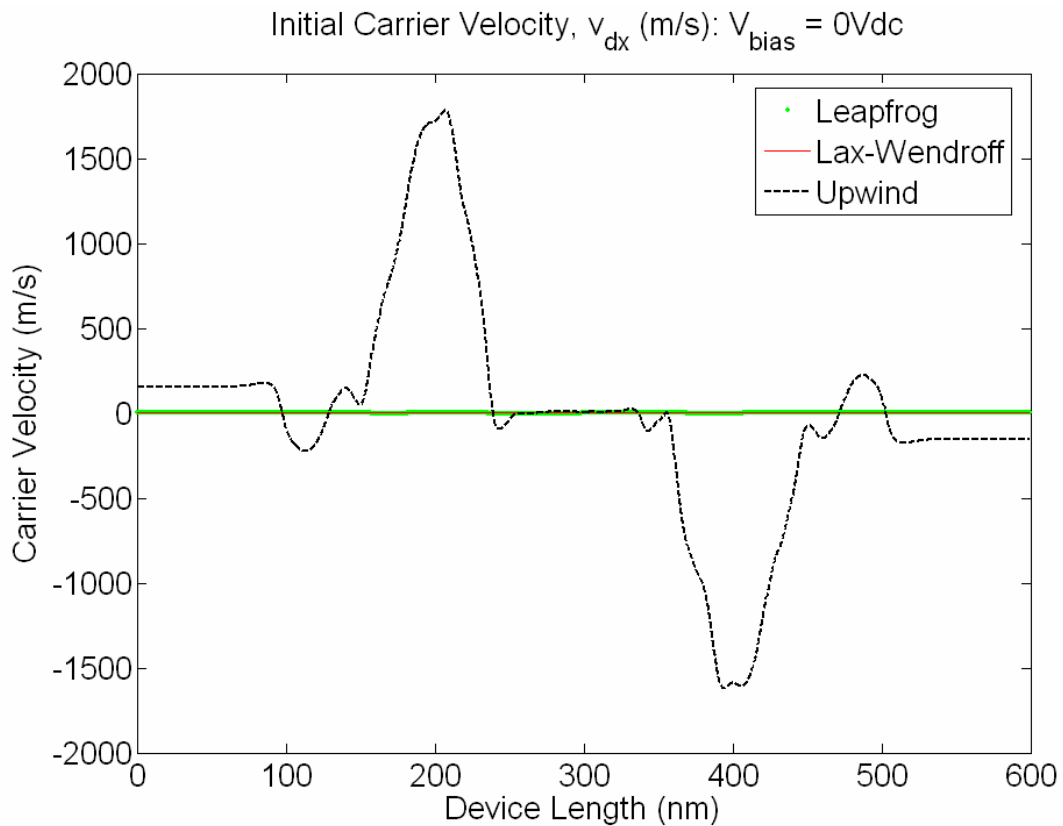


Figure 16: Initial Carrier Velocity Distribution

7.3 Model Stability

Relatively stable initial conditions were obtained for all three models, representing the first of the major hurdles to overcome, shown in Figure 14, Figure 15, and Figure 16 examples. The next level of testing was to apply a reasonable DC bias excitation. A DC bias of 1V DC is considered reasonable and prudent; a much larger voltage could destroy the physical device. 1V DC also seems to be the generally accepted standard test voltage in the representative literature [1, 24,30]. Naively applying a step function to excite the devices under test from 0V to 1V was universally met with divergence of the models, and is simply not realistic. Applying a DC ramp to the system seems most appropriate. Aste & Vahldieck applied a ramp function to their model; however, they

used less than practical 1V/s ramp excitation rate to study the DC conditions. This ramp rate can take months to simulate on even the fastest current PC hardware. As such, this author investigated much faster ramp excitation rates for each model. Figure 17 shows a non-exhaustive ramp rate excitation tolerance of the 3 models. The Leapfrog tolerated a much faster ramp rate than either the Aste & Vahldieck upwind or Lax-Wendroff models. The ramps in Figure 17 represent test cases in which the models successfully stabilized and converged.

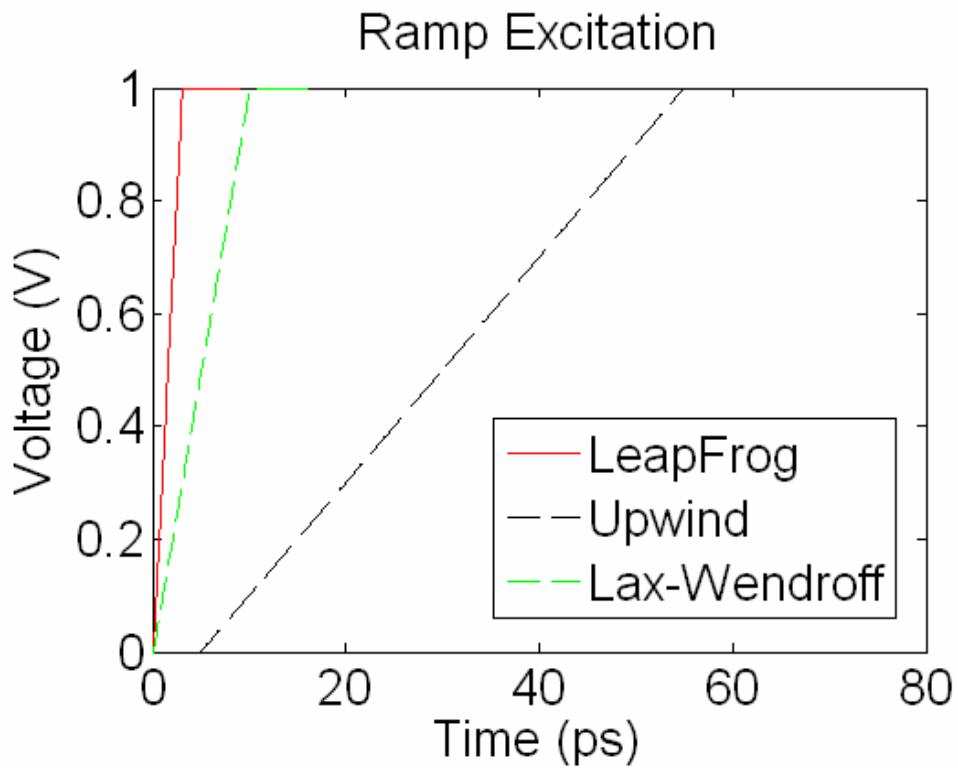


Figure 17: DC bias: Ramp Excitation

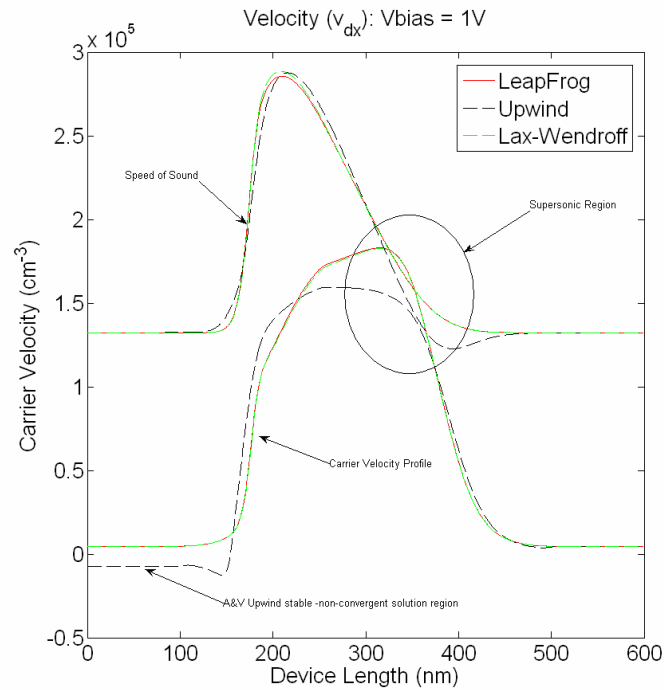


Figure 18: DC bias: Upwind Method Stable but non-convergent

Figure 17 shows the DC bias ramps that were applied to all models that yielded mostly convergent results. The Aste & Vahldieck upwind method is extremely sensitive to the initial conditions; in several tests the results were stable but non-convergent, as seen in Figure 18. According to A&V's approach, the device becomes a perfect sink for electrons as infinite electrons enter the device from both ends. These results are non-physical and a numerical artifact. To solve the problem with the upwind method, the 0V DC initial bias case was allowed to run for ten times longer at 0VDC for the upwind method than both the other models: Lax-Wendroff and Leapfrog. The convergent results can be seen in Figure 19. Figure 18 and Figure 19 have notations showing the calculated speed of sound and the area where expected shockwaves would occur if the simplistic large plasma approximation is used to determine the speed of sound in the device. No shockwaves became apparent in any of the simulations for any discretization. Figure 18

and Figure 19 have areas noted that are expected to have shockwaves forming; however, none form. The most likely cause for this is the speed of sound is incorrectly estimated as the large gas or plasma approximation is not valid. All cases and models had smooth responses for non-exhaustive simulations performed in the development of this work.

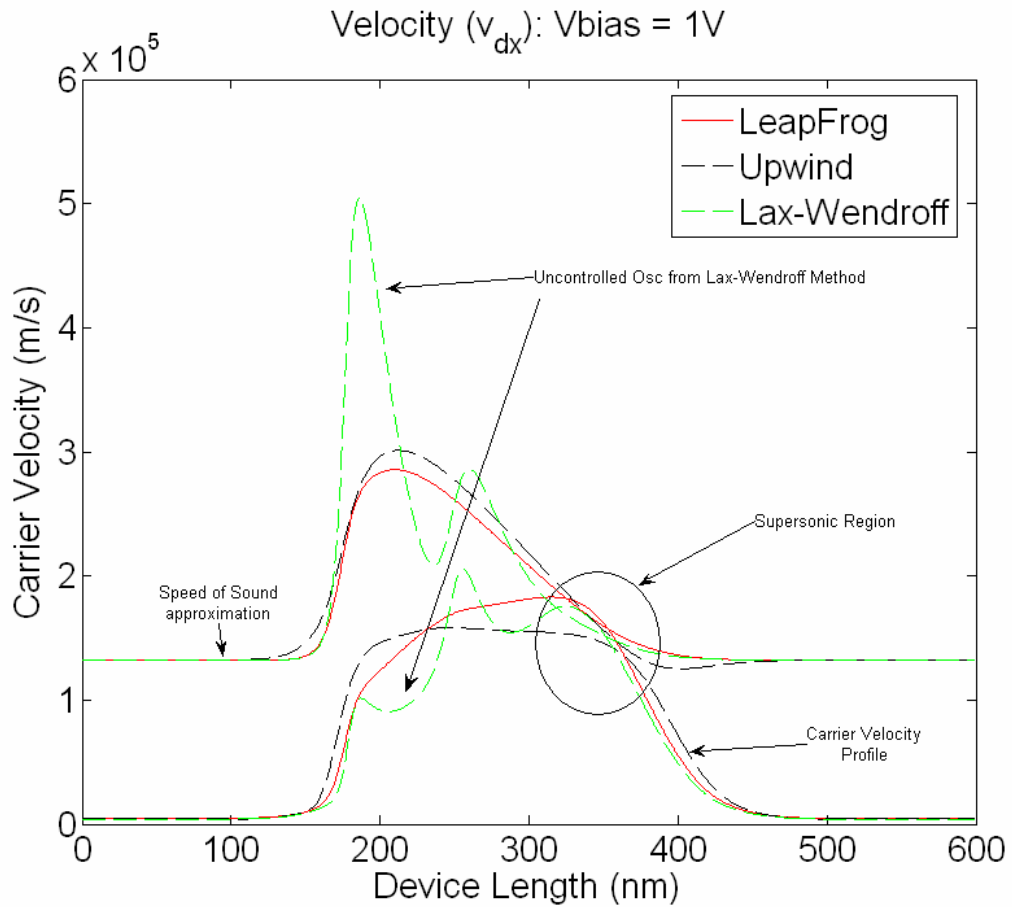


Figure 19: DC bias: Average Carrier Velocity

The Lax-Wendroff method provides relatively stable results for limited time when simulating the device model described in Figure 15, but does not successfully converge. If the simulation time is allowed to continue after the device reaches 1V DC bias for any significant time, the system tends toward uncontrolled oscillations. These oscillations are

expected to be caused by the omission of the diffusion forces caused by the large concentration gradients being omitted from the system of equations. The omission of the diffusive force fails to provide effective dampening forces into the system. Conducted tests showed that as the total device was lengthened, the transition windows were spread, and the differential concentrations were lessened, the model becomes stable and convergent. These results are consistent with the earlier models and devices published by Tomizawa et. Al. [1,2,3,24,30].

Figure 20 through Figure 24 show the results comparing the three models relevant variables at steady state for 1V DC bias. For comparison, the Lax-Wendroff case, that tended to oscillate as the simulation time, went to infinity for $V_{bias} = 1VDC$.

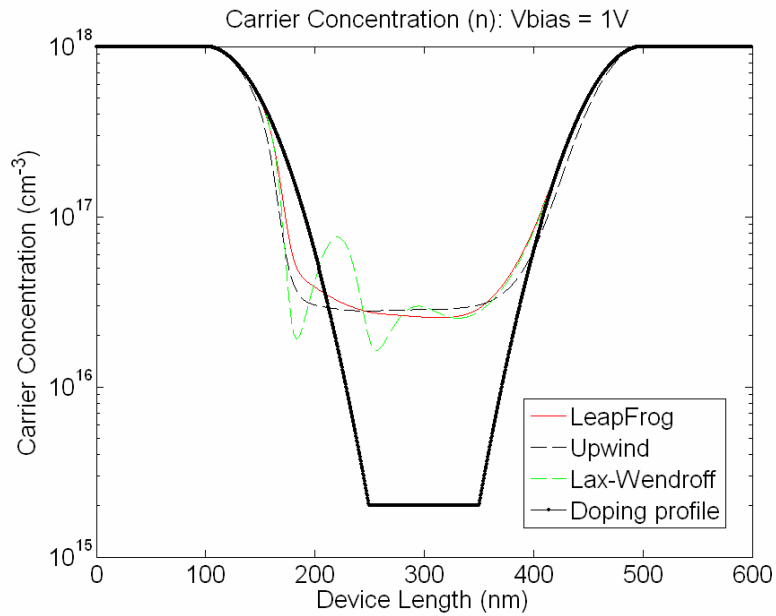


Figure 20: DC Bias: Carrier Concentration Distribution

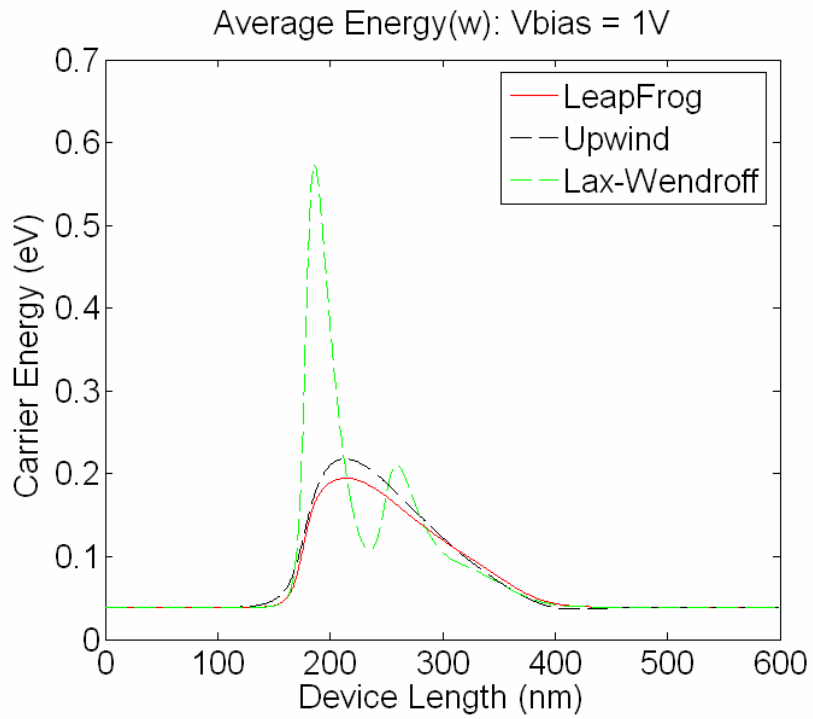


Figure 21: DC bias: Average Energy

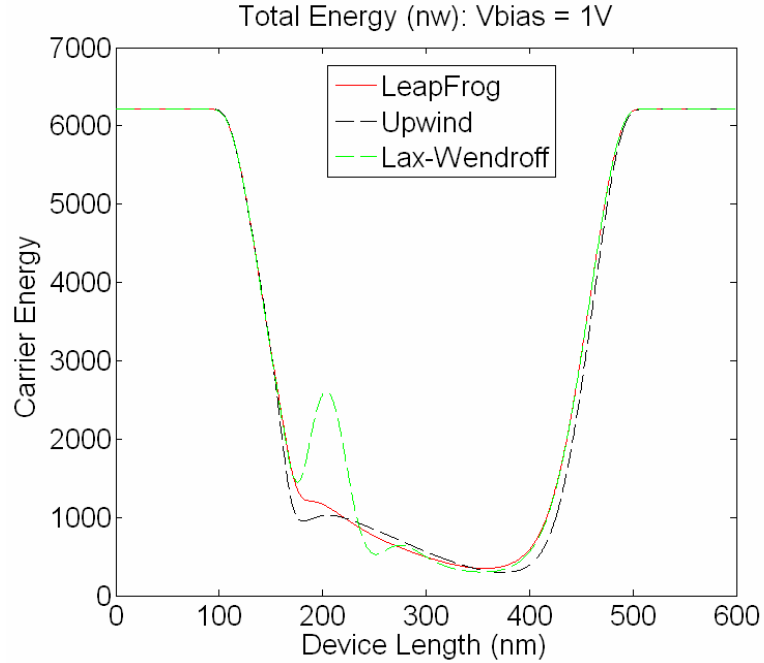


Figure 22: DC bias: Total Energy (n*w)

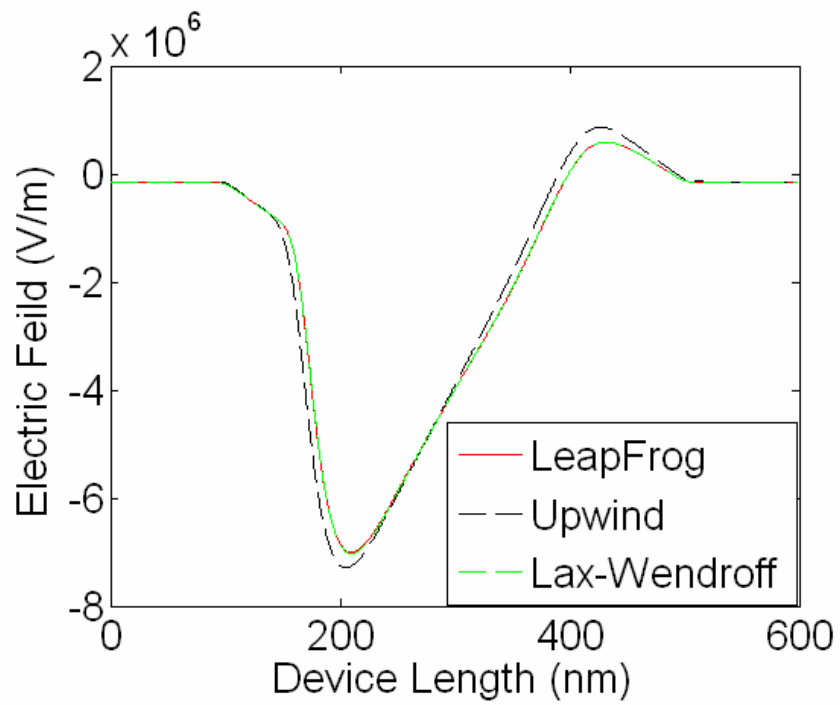


Figure 23: DC bias: Internal Electric Field

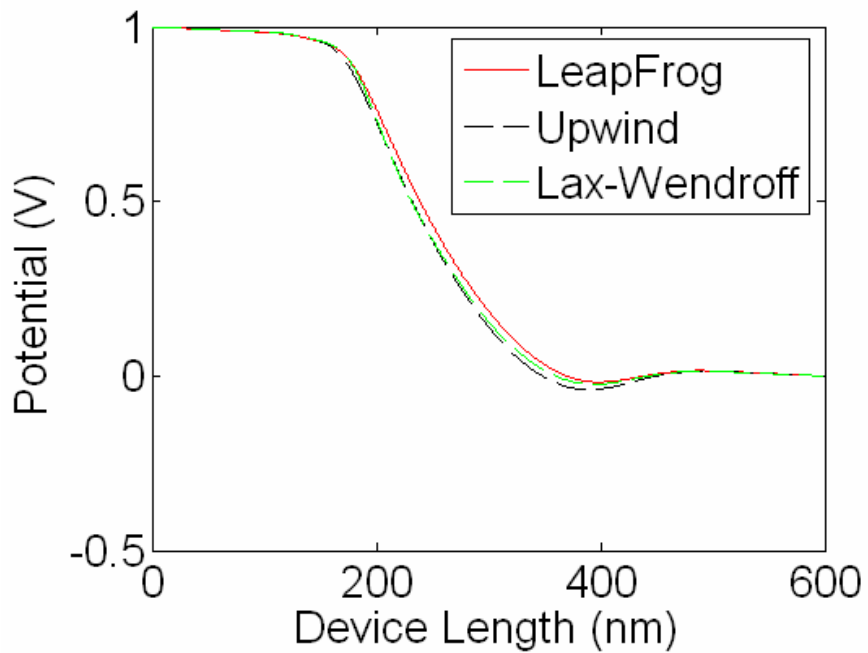


Figure 24: DC bias: Internal Voltage

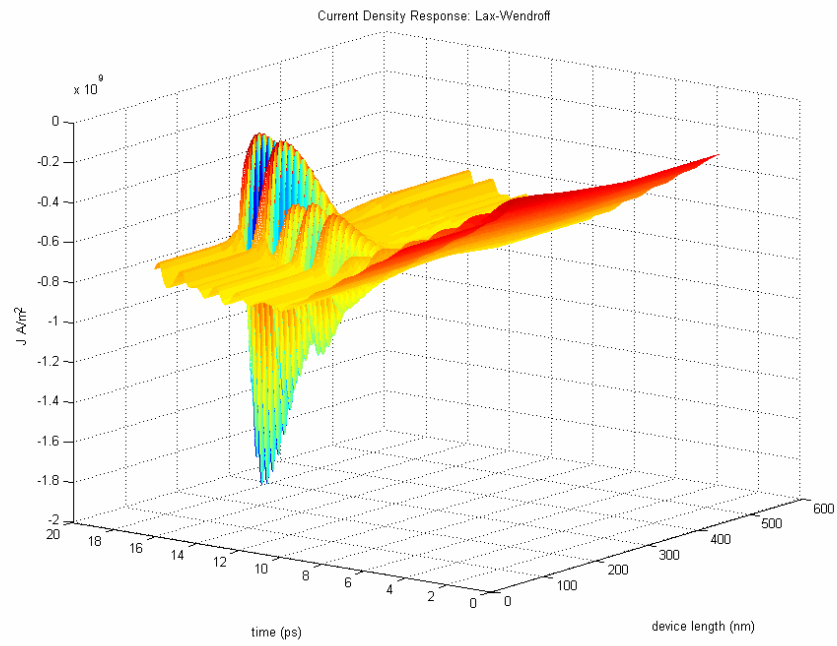


Figure 25: Current Density Response Lax-Wendroff

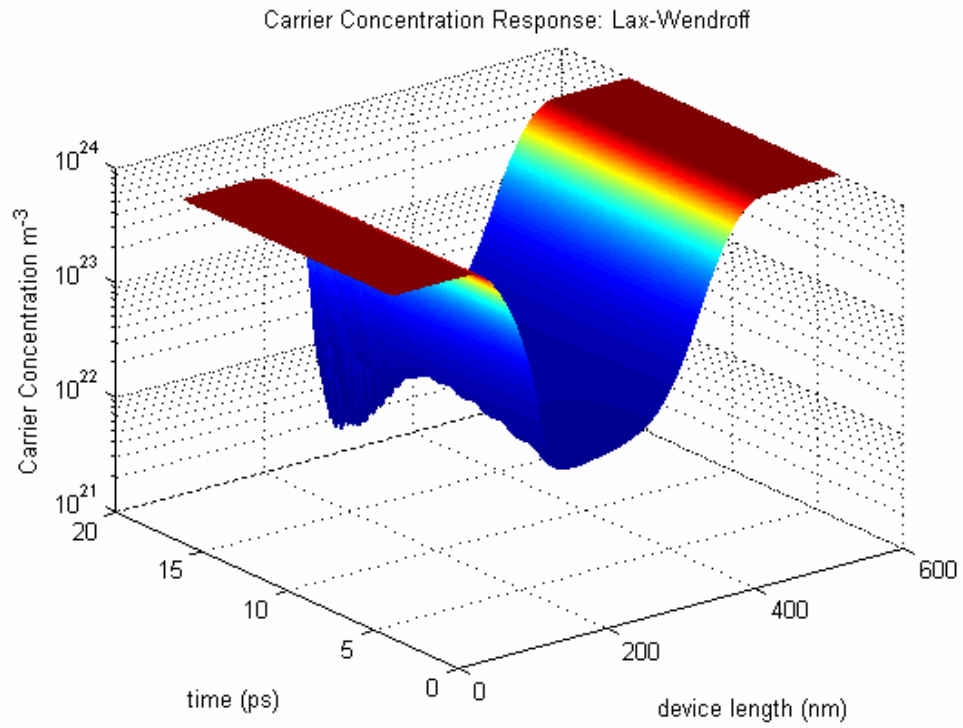


Figure 26: Carrier Concentration Response Lax-Wendroff

Figure 20 through Figure 24 shows the A&V Upwind and the Leapfrog models are very similar in performance for the DC cases. The models all perform well within their expected boundaries. Figure 25 and Figure 26 are surface plots of the response characteristics of the Lax-Wendroff method for the DC bias test case. They show the instabilities of the Lax-Wendroff method for large concentration gradients. While not shown, additional tests were showing the Lax-Wendroff method performs well as the device becomes larger enough that the concentration gradients become a second tier effect. The Aste & Vahldieck upwind method shows slight asymmetries near the boundaries between the source--channel and the channel--drain interfaces as expected, due to the numerical dispersion the method injects into the system. The new Leapfrog method is very similar in performance to the Lax-Wendroff method without the added complexity of discretization of the method, and includes the diffusion terms from the pressure tensor keeping the system stable and convergent for a wider class of problems. The Leapfrog method remains stable for much higher concentration gradients than either the Lax-Wendroff or A&V Upwind method. It was the experience of the author the Leapfrog method was significantly more stable and convergent than the Aste & Vahldieck upwind method or Lax-Wendroff method. The Leapfrog method was often used to determine valid carrier concentration distributions to feed to the other models to determining initial conditions that were both stable and convergent.

7.4 AC results

The Lax-Wendroff method is omitted from further testing because of the problems with respect to convergence for the particular ballistic diode under test. Only the Leapfrog and A&V upwind discretizations results are included from this point forward.

7.4.1 AC excitation method

The signals used to excite the ballistic diode can be seen in Figure 28, Figure 30, and Figure 32. The signal formulation was set to the following. A DC bias was applied for 10% of the period of the excitation frequency. The delay was chosen to give additional margin for the A&V Upwind method stability requirements. The ramp from 0V to 1V was applied over a single period of the excitation frequency. The ramp rate was chosen to test stability and minimize test time. The system is allowed to reach steady state for $\frac{1}{2}$ a period of the excitation frequency, next five sinusoid cycles with 0.2Vpp is summed with the 1V DC bias condition. The piecewise continuous function needs to be discretized in order to be applied as the excitation to an HDM model. The method for discretization is listed below for the example shown in Figure 27.

- **Smooth – HDM:** The excitation function is discretized for each HDM time step in a piecewise step approximation. The time stepping is very small and as such has a very smooth approximation
- **Step – EMS:** Step wise excitation based on the current FDTD-EM calculated applied voltage. The voltage is applied in with a step function and held constant for each EMS-dt.
- **Linear – EMS:** Piecewise linear approximation of the Voltage from the previous FDTD-EM step and the current FDTD-EM time step discretized to the FDTD-EM time step.

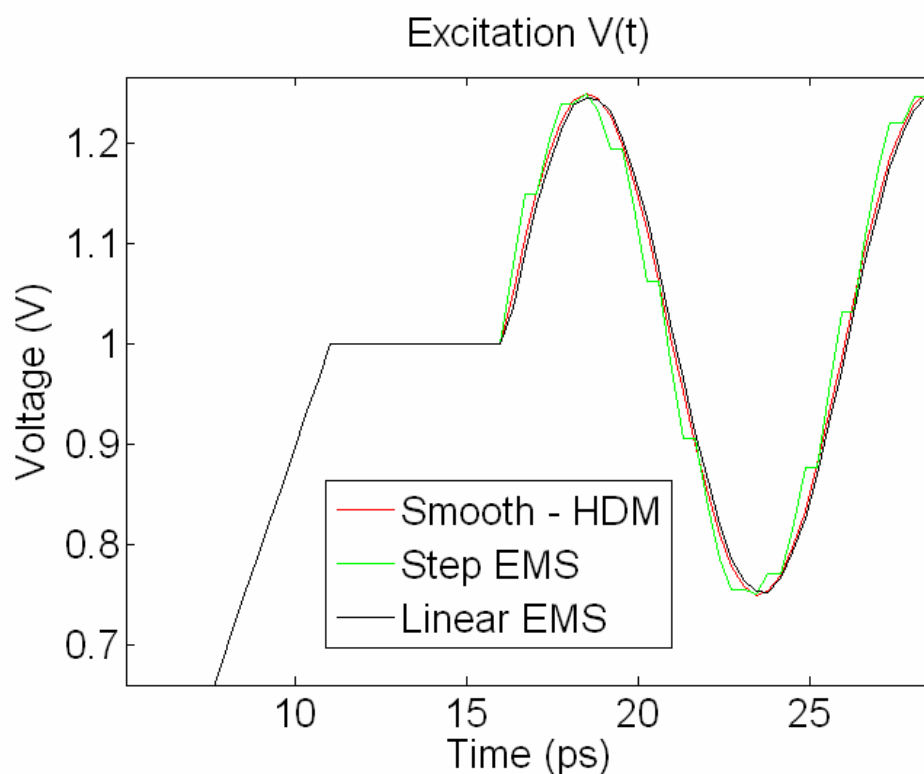


Figure 27: Excitation Methodology

The results from the **Smooth – HDM** test shows that it is a very good approximation of the piecewise continuous function, as expected. The Figure 28 through Figure 33 shows the excitation and resultant current density for the various models and test conditions. The Leapfrog results are shown first followed by the A&V Upwind method results. Each excitation was simulated for all three excitation discretization techniques: **Smooth–HDM**, **Step – EMS**, and **Linear–EMS**.

The Smooth–HDM method shows very smooth results, but requires a-priori knowledge of the input signal. It is not practical for embedding in a FDTD-EM simulator, but is excellent for comparing the results of other excitation discretization methods. The Step – EMS method is very practical for embedding into a FDTD-EM tool as it only requires

information regarding the current EMS time step information; however as can be seen in the figures the step excitation produces non-physical effects in the device response. The Linear—EMS method produces results very consistent with Smooth-HDM. The method is excellent for embedding as it only requires the current time step and the last time step excitations to perform the linear interpolation for all intermediate HDM time-steps, without adding a significant computational overhead to the FDTD-EM algorithm.

7.4.2 Leapfrog Results

The results of the Leapfrog discretization of the HDM are presented first. Results for the tests of 500GHz, 100GHz, and 20GHz RF excitation signals for all three excitation discretization methods are presented.

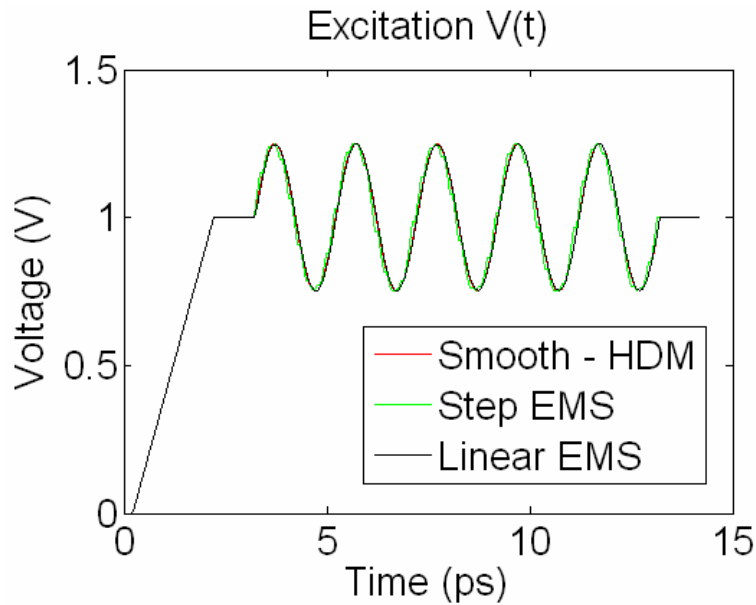


Figure 28: 500GHz Excitation Leapfrog Method

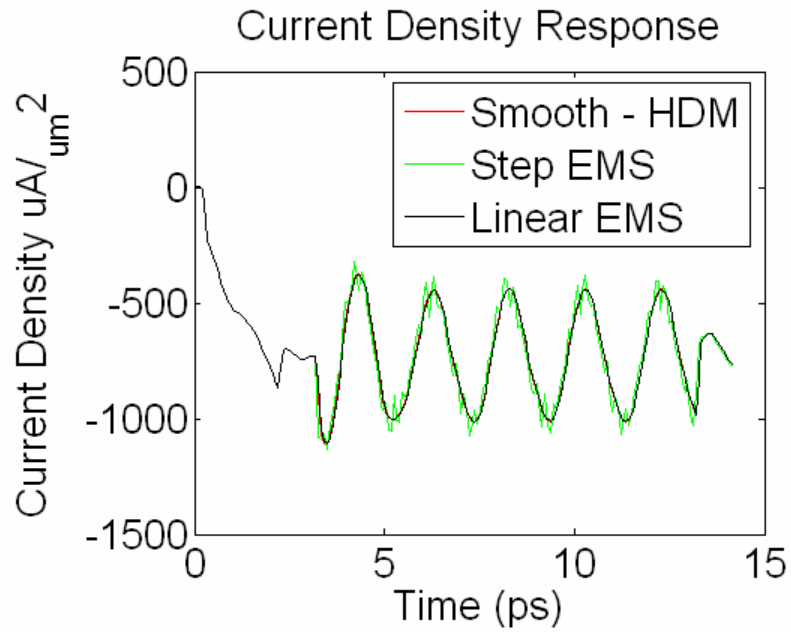


Figure 29: 500GHz Excitation Leapfrog Method

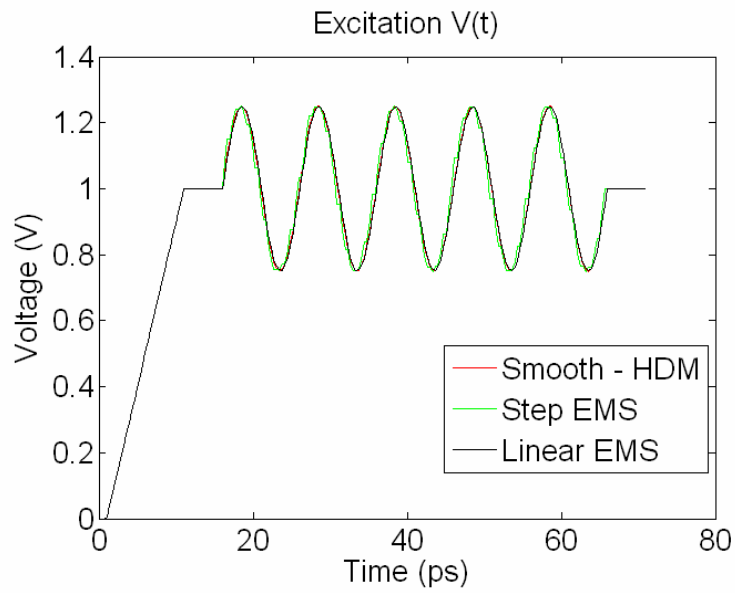


Figure 30: 100GHz Excitation Leapfrog Method

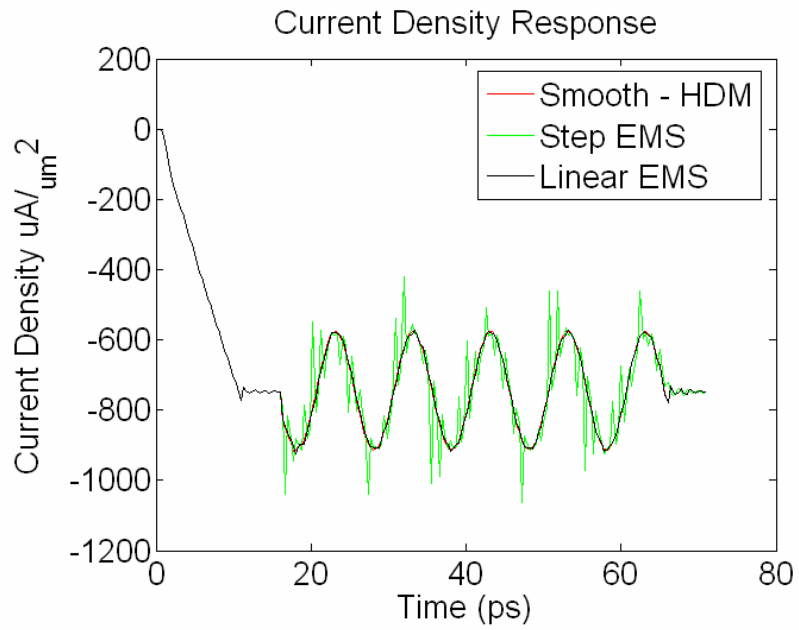


Figure 31: 100GHz Response Leapfrog Method

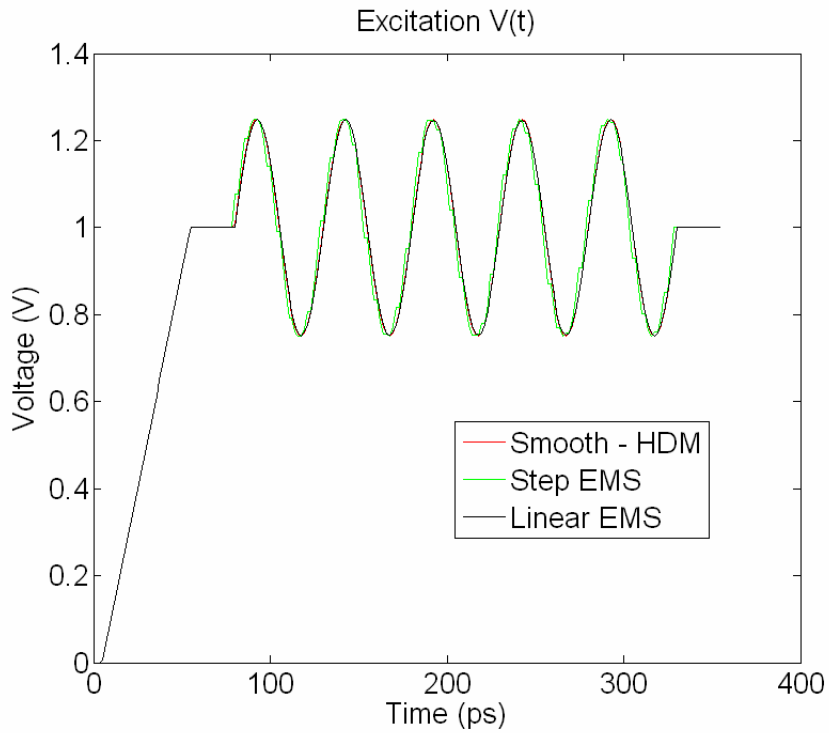


Figure 32: 20GHz Excitation Leapfrog Method

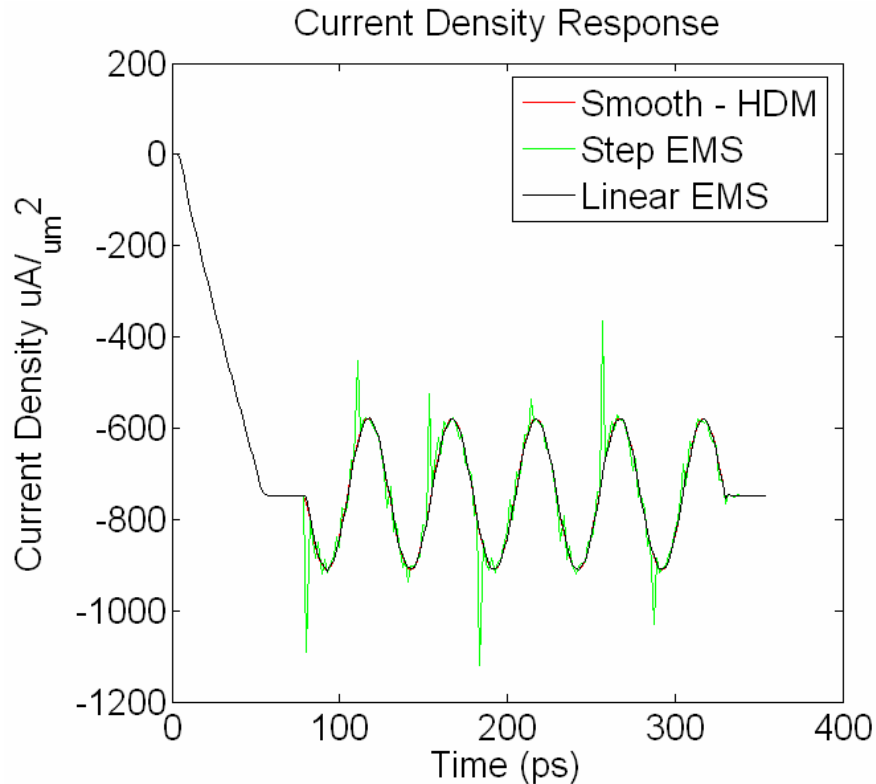


Figure 33: 20GHz Response Leapfrog Method

As can be seen in Figure 29, Figure 31, and Figure 33, the **Step—EMS** excitation produces significant deviations from the reference **Smooth—HDM** excitation method. The **Linear—EMS** method produces results that are very consistent with the **Smooth—HDM** method. The **Step—EMS** excitation produces significant disturbances from the **Smooth—HDM** most likely cause by the Poisson equation effects. The disturbances are numerical artifacts not physical effects.

7.4.3 Aste & Vahldieck Upwind Method Results

The next set of excitations and resultant current densities represent the identical tests to those performed on the Leapfrog discretization, but for the Aste & Vahldieck upwind method to discretize the HDM. The amplitude of the deviations from the baseline **Smooth—HDM** appears to be larger for the upwind method than the Leapfrog method.

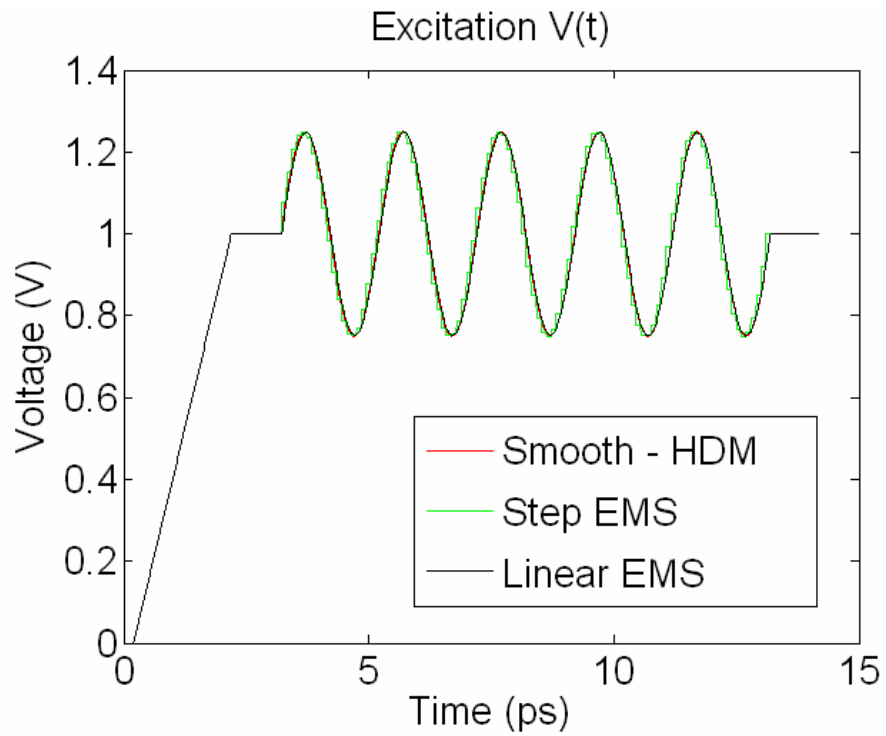


Figure 34: 500GHz Excitation A&V Upwind Method

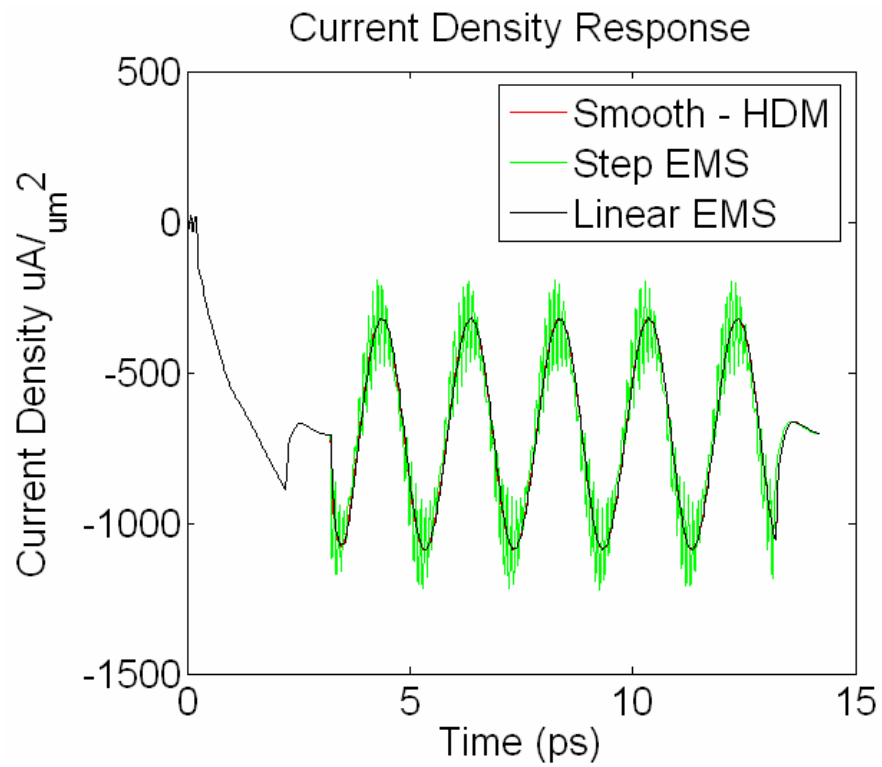


Figure 35: 500GHz Excitation A&V Upwind Method

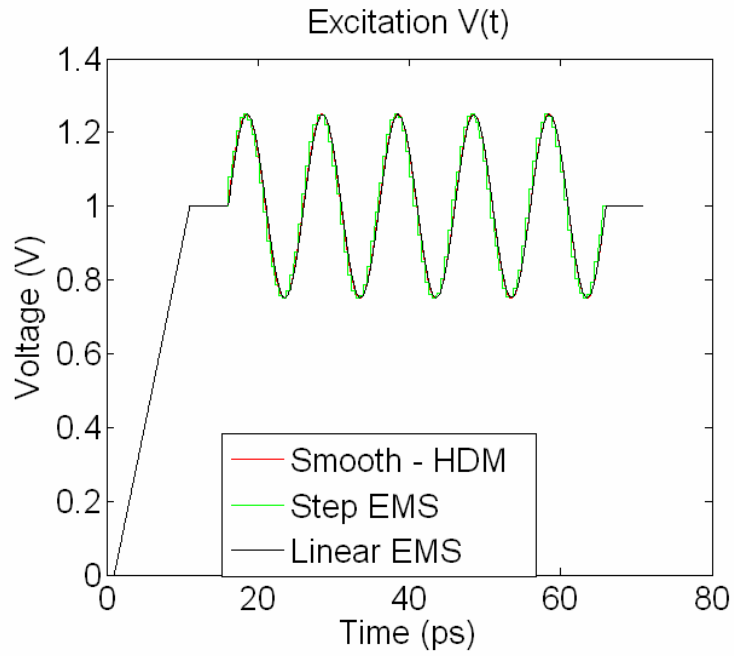


Figure 36: 100GHz Excitation A&V Upwind Method

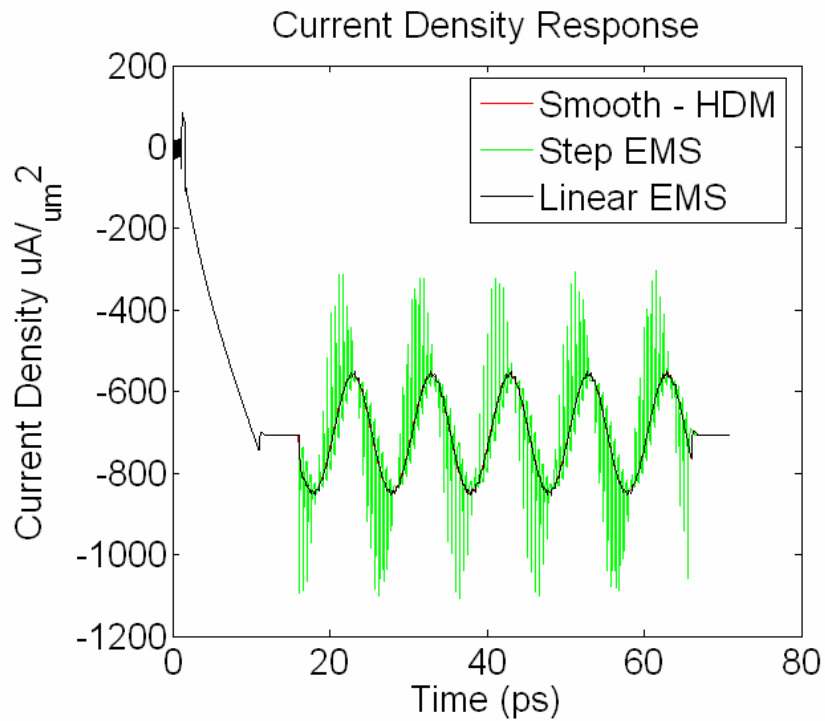


Figure 37: 100GHz Excitation A&V Upwind Method

7.4.4 Comparison of HDM Discretization Methods

Comparing the models' results together shows the similarities and differences between the two HDM discretizations. Both models produce similar results, thereby validating the new Leapfrog method. The upwind method has significant dampening when excited; however, for the equilibrium case it suffers from oscillations as can be seen in the first several picoseconds in Figure 38. The Leapfrog method produces results consistent with theory. The trailing edge of the excitation shows as damped oscillation. The negative value of the current density has to do with the direction of current flow. Current flow is assumed to be positive in the +z direction. The biasing of the diode caused the current flow in the negative direction. Current density is a vector; as such it has a magnitude and direction.

The most interesting result is the superior performance of a simple piecewise linear approximation of the excitation signal. The results do show some susceptibility to the slope changes in the excitation; however they are insignificant as compared to the piecewise step excitation. This demonstrates some of the inherent limits of trying to use DC bias curves to predict the AC response of an active non-linear device. Figure 39 shows a zoomed in area of the results comparison for closer examination. The stability characteristics of the Leapfrog method coupled with the excellent results for the **Linear-EMS** excitation coupling method make the de-coupling of the FDTD-EM and FDTD-HDM grids possible. Practically, this allows for the embedding of the complex FDTD-HDM tool into a single cell of the EM grid. A specific example would be embedding a nano-scale device into an FDTD-EM grid of 100x100x100. Computational savings are on the order of 10^{16} for each time step of a 100x100x100 FDTD-EM grid discretized for 200GHz.

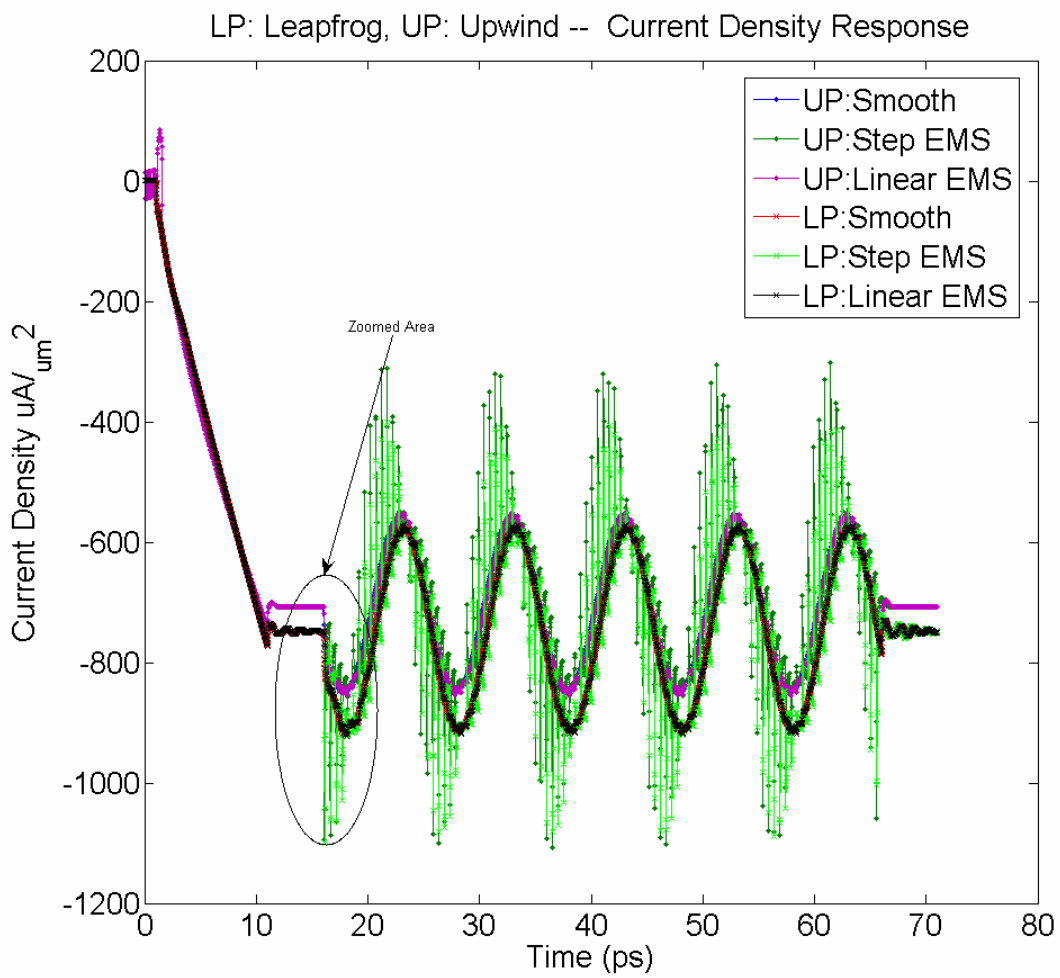


Figure 38: 100GHz Response Leapfrog and Upwind Methods

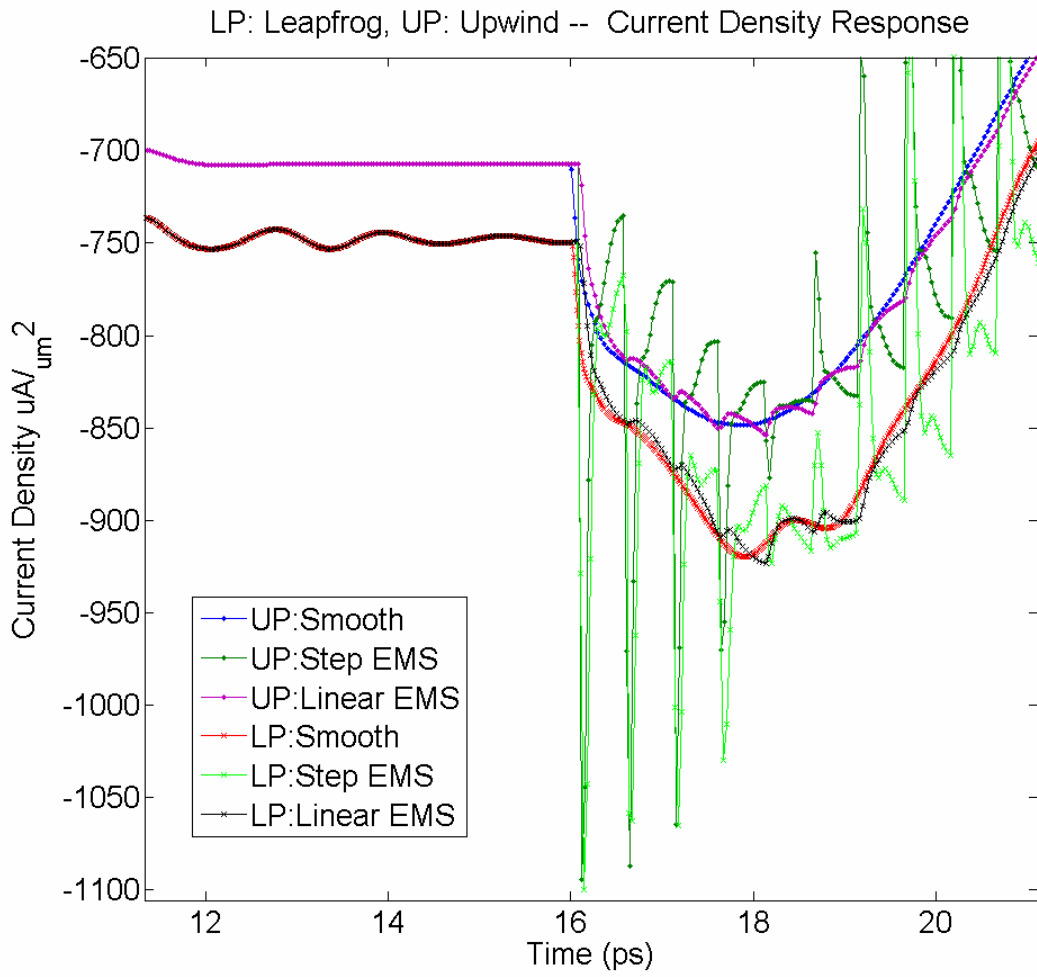


Figure 39: Zoomed from previous image

Method	Time Step (sec)	Space Step (m)	Max Velocity (m/s)	Cells
Lax-Wendroff	2.04e-17	4.08e-10	2e7	1467
A&V Upwind	2.04e-17	4.08e-10	2e7	1467
Leapfrog	4.08e-17	4.08e-10	1e7	1467

Table 1: HDM Gridding

Method	RF Excitation	Total Time steps
A&V Upwind	20GHz	17 million
	100GHz	3.4 million
	500GHz	0.7 million
Leapfrog	20GHz	8.6 million
	100GHz	1.7 million
	500GHz	0.3 million

Table 2: HDM Time steps for RF Excite Tests

Method	RF Excitation	EMS Time step (sec)	HDM time steps per EMS time step	EMS space step (m)	HDM Length (m)
A&V Upwind	20GHz	2.5e-012	125000	750e-6	600e-9
	100GHz	5e-013	24999	150e-6	600e-9
	500GHz	2.5e-013	12499	75e-6	600e-9
Leapfrog	20GHz	2.5e-012	61274	750e-6	600e-9
	100GHz	5e-013	12254	150e-6	600e-9
	500GHz	2.5e-013	6127	75e-6	600e-9

Table 3: Compare HDM and EMS

Table 1 shows that all the different discretization techniques have uniform spatial discretization. The $1/10^{\text{th}}$ the Debye length determines the spatial gridding, as all the devices under test were uniform; no variation is expected. The time step for the HDM model is determined by the CFL condition shown in 4.3.1. The maximum average velocity of the carriers is related to the time step. It was found that the Leapfrog method remained stable with a maximum velocity $\frac{1}{2}$ of the value required for both the Lax-Wendroff and A&V Upwind method. The stable value still met the CFL condition requirement. Table 2 tabulates the parameters used test the two different methods in the AC section of the results. Table 3 shows computational requirements and relationship between the two models.

CONCLUSION

A new and novel method for coupling a FDTD-EM and FDTD-HDM models has been presented removing the previous requirement for a unified spatial and temporal grid between the models. Decoupling the grids leads to significant computational savings. For practical RF devices (<200 GHz) the computational savings is approximately 10 orders of magnitude per FDTD-EM cell per FDTD-EM time step as the HDM can be typically embedded in a single FDTD-EM cell. This reduces each of the models to their respective CFL conditions instead of imposing the smallest CFL condition on both models.

The newly proposed discretization methodology for the FDTD-HDM expands Yee's Leapfrog method to an entirely new class of problems. The method has proven to be more stable and convergent than other state-of-the-art discretization schemes. Coupling the new discretization method with the well defined coupling methodology opens the field to entirely new classes of problems that can be simulated.

REFERENCES

-
- 1 Tomizawa K., *Numerical Simulation of Submicron Devices*, Norwood Ma: Artech House Inc, 1993.
 - 2 Taflove, A. El-Ghazaly, S., *Advances in Computational Electro-dynamics: The finite-difference time domain method*, Norwood, Ma: Artech House Inc, 1988.
 - 3 Imitaz, S., M., S, El-Ghazaly, S., "Global Modeling of Millimeter-Wave Circuits: Electromagnetic Simulation of Amplifiers," *IEEE Trans. on Microwave Theory and Techniques*, vol. 45, no. 12, 1997, pp.2208-2216
 - 4 McGarvey, B., Tentzeris, M., "Coupling of Solid-State and Electromagnetic Equations for Simulation of Wireless Packaged Geometries", *Proc. of the 2001 European Microwave Symposium*, London, England, September 2001, pp.217-220. (vol.I).
 - 5 BlotekJaer, K, "Transport Equations for Electrons in Two-Valley Semiconductors," *IEEE Trans. On Electron Dev.* Vol. 12, pp. 38-47, 1970.
 - 6 Yee, K. S., " Numerical solutions of initial boundary value problem involving Maxwell's equations in isotropic media," *IEEE Trans. Antennas and Propagation*, vol 14, 1966, pp. 302-307
 - 7 Bohm, D, *Quantum Theory*, New York, NY, Dover Publications, 1951
 - 8 Taflove, A. Picket-May, M, et. al., *Advances in Computational Electro-dynamics: The finite-difference time domain method*, Second Edition, Norwood, Ma: Artech House Inc, 2000
 - 9 Atkins, P., *Physical Chemistry, 6th Edition*, New York, NY, W. H. Freeman and Company, 1998
 - 10 University of Washington N-body Shop <http://www-hpcc.astro.washington.edu/>
 - 11 Anile, A.M.; Liotta, S.F.; Mascali, G.; Rinaudo, S., "Two dimensional MESFET simulation of transients and steady state with kinetic based hydrodynamical models," *Computational Electronics*, 2000, IWCE Glasgow 2000. 7th International Workshop on 22-25 May 2000, pp.124 - 126
 - 12 Brunetti, R., Jacoboni, C., Nava, F., Reggiani, L., Bosman, G., Zijlstra, R. J. J., "Diffusion coefficient of electrons in silicon", *J. Appl. Phys.*, **52**(11), November 1981
 - 13 Jacoboni, C., Reggiani, L., "The Monte Carlo method for the solution of charge transport in semiconductors with applications to covalent materials," *Reviews of Modern Physics*, Vol. 55, No 3. July 1983

-
- 14 Pierret, R. F., *Semiconductor Device Fundamentals*, New York, NY, Addison-Wesley Publishing Company, 1996
- 15 Serway, R., A., *Physics for Scientists & Engineers with Modern Physics*, Philadelphia, PA, Saunders College Publishing, 1996
- 16 Chen, F., *Introduction to Plasma Physics and Controlled Fusion*, New York: Springer, 2nd Ed. 2006.
- 17 Yougrau, W., Mandelstam, S., *Variational Principles in Dynamics and Quantum Theory*, New York, NY, Dover Publications, 1968
- 18 Schrodinger, E., *Statistical Thermodynamics*, New York, NY, Dover Publications Inc., 1989
- 19 Wannier, G. H., *Statistical Physics*, New York, NY, Dover Publications Inc., 1996
- 20 Landau, L.,D., Lifshitz, E.,M., *Electrodynamics of Continuous Media 2nd Edition*, Oxford, UK, Elsevier, 2006
- 21 Sze, S. M., *Physics of Semiconductor Devices*, New York, NY, John Wiley & Sons, 1981
- 22 Boltzmann, L., Translated Brush, S., G., *Lectures on Gas Theory*, New York, NY, Dover Publications Inc., 1964
- 23 Maxwell, J., C., *Theory of Heat*, New York, NY, Dover Publications Inc., 2001
- 24 Aste, A, Vahldieck R., "Time-domain simulation of full hydrodynamic model," *Int. J. Numer. Model.* 2003; 16:161–174.
- 25 Baccarani G. and Wordeman M.R., "Investigation of steady-state velocity overshoot in Silicon," *Solid-State Electronics*, Vol 28, 1985, pp. 407-416.
- 26 Blotekjaer, K., "High-frequency conductive, carrier waves, and acoustic amplification in drifted semiconductor plasmas," *Ericsson Technics*, vol. 22, pp 125-183, Oct 1966
- 27 Landau L., Lifshitz E., *Fluid Mechanics 2nd Edition*, Oxford, UK, Elsevier, 2004
- 28 Alsunaidi, M.A. , Hammadi, S.M., El-Ghazaly, S.M, "A parallel implementation of a two-dimensional hydrodynamic model for microwave semiconductor device including inertial effects in momentum relaxation," *Int J. Num. Mod.:Netw. Dev. Fields*, Vol 10, pp. 107-119, 1997
- 29 Krall, N.A., Trivelpiece, A. W., *Principles of Plasma Physics*, San Francisco, CA, San Francisco Press, Inc, 1986

-
- 30 Aste, A., Vahldieck, R., Rohner, M. "Full hydrodynamic simulation of GaAs MESFETs," *Int. J. Numer. Model.* 2004; 17:43-59
- 31 R. A. Stewart, Liangxiu Ye, J. N. Churchill, "Improved Relaxation Time for Two-Band Hydrodynamic Models," *Solid State Electronics*, Vol 32, No. 6, pp 497-502, 1989
- 32 Oran, E., S., Boris, J. P., *Numerical Simulation of Reactive Flow*, New York, NY, Elsevier Science Publishing, Inc., 1987
- 33 Jones, W., March, N., H., *Theoretical Solid State Physics: Volume 1: Perfect Lattices in Equilibrium*, New York, NY, Dover Publications, 1973
- 34 Ulaby, A. T., *Fundamentals of Applied Electromagnetics*, Upper Saddle River, NJ, Prentice Hall, 1997
- 35 Cheng, D., *Field and Wave Electromagnetics*, Reading, MA, Addison-Wesley Publishing Company, 1992
- 36 Huba, J. D., 2004 revised, *NRL Plasma Formulary*, Naval Research Laboratory, Washington DC, 20375
- 37 Taflove, A, et. al., *Advances in Computational Electro-dynamics: The finite-difference time domain method, Second Edition*, Norwood, Ma: Artech House Inc, 2000.
- 38 McGarvey Submitted MWCL 2007
- 39 Taflove, A. et. al., *Computational Electrodynamics: The Finite-Difference Time-Domain Method*, Boston, MA, 1995